J. Fluid Mech. (1966), *vol.* 26, *part* 2, *pp.* 337–368
Printed in Great Britain

The flow of a jet from a body opposing a supersonic free stream

By P. J. FINLEY
Engineering Department, Cambridge University†

(Received 27 August 1965 and in revised form 10 December 1965)

A series of experiments is described in which a jet issues from an orifice at the nose of a body in supersonic flow to oppose the mainstream. An analytical model of the flow is developed which suggests that the aerodynamic features of a steady flow depend primarily on a jet flow-force coefficient, and the Mach number of the jet in its exit plane. A sufficient condition for steady flow is developed. The experiments are found to agree well with predictions based on the flow model. A short account is presented of some previous investigations, and some of their conclusions are re-examined in the light of the present study.

1. Introduction

A body immersed in a high-velocity gas stream is subjected to high temperatures and pressures over its forward-facing surfaces. Various authors have suggested that the pressure and temperature distributions might be modified with advantage by the introduction of a secondary flow at or near the front stagnation point of the body.

Baron & Alzner (1963) have described a theoretical and experimental investigation of an attached 'shock cap', originating as a source flow within the body, and forming a thin layer of fluid over the body nose. This might be utilized to provide a protecting blanket of low temperature fluid in hypersonic flight. An experimental investigation with the same aim has been made by Warren (1960), in which the secondary flow originated in a separated jet opposing the mainstream. Lopatoff (1951) and Love (1952) have shown that a separated jet modifies the pressure distribution so as to reduce the pressure drag of the body. In these investigations the ratio of the body diameter d_m to the jet diameter d_j (see figure 1) is large, of the order 20. Other practical investigations in which the jet diameter is of the same order as that of the body are described by Watts (1956) and Romeo & Sterret (1963).

These investigations have shown that a low-velocity 'dead-air' region surrounds the jet and that the bow shock is displaced forwards. The pressure in the dead-air region is markedly lower than the stagnation-region pressures of the same body with no jet. In general the bow shock moves forward and the dead air region pressure drops as the total pressure of the jet increases. Romeo & Sterret have shown that the flow tends to be very unsteady when the jet total pressure is low and the jet is small as compared to the body from which it issues.

† Present address: Engineering Department, University of Malaya, Kuala Lumpur.

Steady flows are found with large jets and high jet total pressures, when the jet has a single cell terminated by a strong shock. These previous studies together cover a wide range of variables, but do not indicate how the observed phenomena may be predicted, or correlated on a simple basis. The present study is intended to accomplish this for flows in which the jet separates from the body surface.

2. Controlling parameters

Figure 1 shows a jet issuing from a body against a supersonic airstream. The bow shock stands away from the body surface, and takes a form appropriate to a new body consisting of the original body with a protrusion due to the jet flow. The boundary of this protrusion is defined by the *interface*, the stream surface between the jet flow and the mainstream flow.

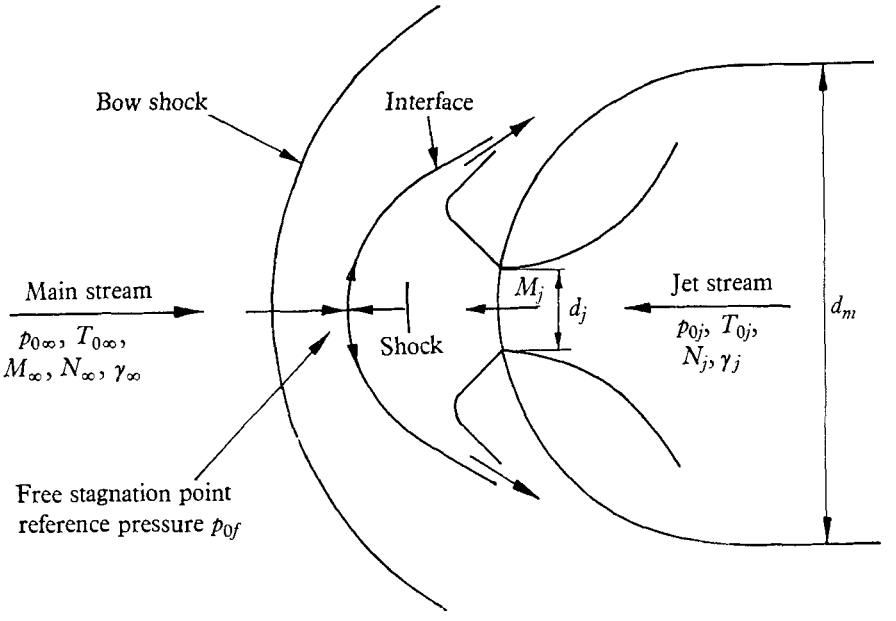

FIGURE 1. Principal features of the flow, and independent variables.

It will be assumed that the flow is axially symmetrical throughout, that the jet and the mainstream consist of perfect gases, and that the jet is uniform, and parallel in its exit plane. The scale is assumed to be such that variations of Reynolds number may be neglected, and no account is taken of heat transfer to or from the body. The independent variables are then those which specify the size and shape of the body and nozzle, and the aerodynamic properties of the jet and the free stream.

The experimental investigation was restricted to separated jets issuing along the axis of a family of spheroids of elliptic meridian section. This includes all shapes tested by other workers excepting Baron & Alzner (1963), who were primarily interested in an attached flow. The body shape and size are then specified by the fineness λ and the body diameter D, defined by

$$\lambda = a/b, \quad D = d_m/d_j,$$

where a, b are the semi-axes of the elliptical section parallel and normal to the free stream and d_m ($= 2b$) is the nose-shape diameter. The diameter d_j of the jet is chosen as the reference linear dimension throughout the paper.

The properties of the free stream and the jet are specified by their specific-heat ratios, γ_j for the jet and γ_∞ for the free stream, and by the ratio N of their molecular numbers N_j and N_∞. For dynamic similarity it is also necessary to state the free-stream Mach number M_∞ and the jet Mach number M_j. It remains to specify the jet total-pressure ratio P and the total-temperature ratio T, given by

$$P = p_{0j}/p_{0f}, \quad T = T_{0j}/T_{0\infty},$$

where p_{0j} is the jet total pressure, p_{0f} is the Pitot pressure of the free stream, T_{0j} is the jet total temperature and $T_{0\infty}$ the free-stream total temperature, taken as the reference temperature.

The free-stream Pitot pressure p_{0f}, the total pressure after a normal shock, is chosen as the reference pressure. At high free-stream Mach numbers, the pressure on a blunt body is given closely by Newtonian theory. The local surface pressure then depends primarily on p_{0f} and the local surface inclination. Watts (1956) showed that the interface was blunt for large jets.

An interface of given shape thus implies a given pressure distribution, only slightly dependent on M_∞, and virtually independent of the other free-stream quantities $T_{0\infty}$, γ_∞, N_∞. A given jet flow within a given interface may therefore be exposed to a range of supersonic streams of high Mach number, and, if p_{0f} remains constant, changes of free stream will only have a slight effect on the pressure field, mainly through changes in the development of a mixing layer on the interface.

The principal independent parameters of dynamically similar flows are thus the non-dimensional body diameter D, the body-shape fineness λ, the jet total-pressure ratio P, the jet exit-plane Mach number M_j, and the jet-gas specific-heat ratio γ_j.

The parameters N, γ_∞, T are expected to affect mixing processes, and so control transfer of heat to or from the body. This aspect is not being studied here. If M_∞ is large they will have little influence on the main aerodynamic aspects of the flow. The influence of M_∞ will be demonstrated by the analysis.

3. Experimental arrangements

All measurements were made in an intermittent wind tunnel with a rectangular (6·25 in. × 4·5 in.) working section. The free stream properties were:

$$M_\infty = 2{\cdot}5, \quad p_{0\infty} = 40 \text{ psia}, \quad T_{0\infty} = 530\,^\circ\text{R},$$

giving a free-stream Reynolds number of 7×10^5 per inch. The models were hemisphere-cylinders of 2 in. diameter, or cylinders 1 in. in diameter, with spheroidal noses of various shapes. Air for the jet came from the tunnel supply through a diaphragm control valve so that the total pressure could be held constant in the range $20 < p_{0j} < 250$ psia. P thus lay in the range $1 < P < 12{\cdot}5$. The total temperatures of the two streams were uncontrolled, but both were found to be very close to room temperature (approximately 530 °R). Thus $T \simeq 1$.

In some experiments carbon dioxide from a commercial cylinder was ducted to the jet instead of air, when the temperature fell below room temperature but was not controlled or measured.

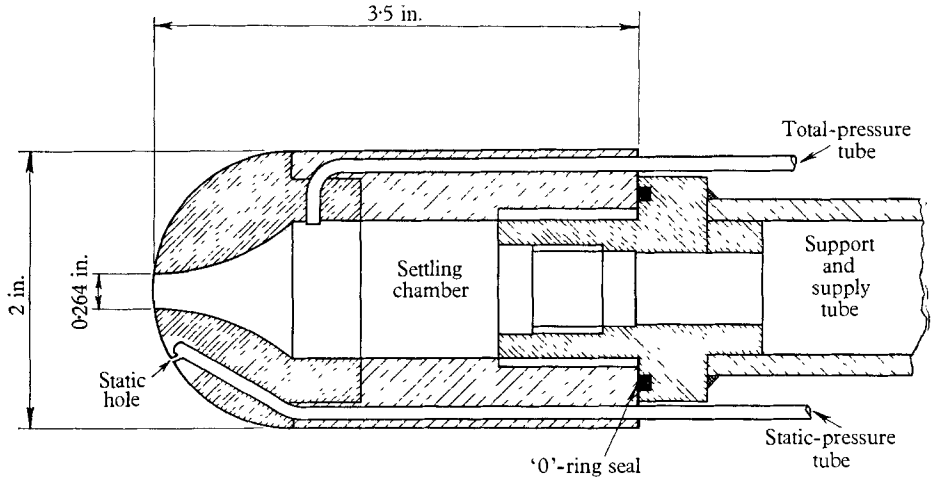

FIGURE 2. Section of one of the 2 in. diameter models.

Figure 2 shows the construction of one of the 2 in. diameter models. The nose contains a convergent passage leading to the orifice, finishing in a short parallel section with a sharp lip, so that M_j was 1. The values of D were 7·6, 16·4 and 33·3. A 5° conically divergent nozzle was also constructed such that the flow, if assumed one-dimensional, emerged at $M_j = 2{\cdot}6$. For this nozzle $D = 9{\cdot}4$. These models had static-pressure holes distributed in a spiral on the spherical surface (for location see figure 5), and an internal total-pressure tapping, shown in figure 2.

The 1 in. diameter spheroids had a contraction leading to a plug in which the nozzle was formed. This plug was drilled out and replaced to vary D in the range $3{\cdot}5 < D < 35$. There was a single static hole adjacent to the plug, and the jet total pressure was measured internally. The exterior shapes were spheroids such that $\lambda = 0,\ 0{\cdot}5,\ 1,\ 2$. A special model with an outside diameter of $\frac{5}{16}$ in. was constructed for the case $\lambda = 0$, $D = 1{\cdot}67$.

The accuracy of pressure measurement was governed by the accuracy with which the tunnel total pressure could be controlled, estimated at 0·75 %. The tunnel total pressure was measured on a test-quality bourdon-tube gauge. The jet total pressure was measured on a bourdon-tube gauge or a mercury manometer. Static pressures were recorded on a multitube mercury manometer in tests lasting 20 sec.

The flow field was found to vary discontinuously with P, so provision was made for recording the variation of a static pressure with the jet total pressure electrically. Static pressure and total pressure signals were fed to strain-gauge pressure transducers to give D.C. signals which were fed to the axes of an X–Y chart plotter. The plot of static pressure as a function of jet total pressure obtained agreed with the manometer measurements. All pressure measurements quoted

are accurate to 1 %. A conventional single-pass schlieren and shadowgraph system was used.

Further details of the experimental arrangements are given by Finley (1963), with the full results, from which a selection is now described.

4. General description of the flow

Figure 3 shows the main features of the flow field as deduced from schlieren photographs such as figure 4, plate 1.

The *jet A* separates from the sharp-edged orifice and moves forward to an *interface B* with the mainstream. There is a toroidal recirculation region, the

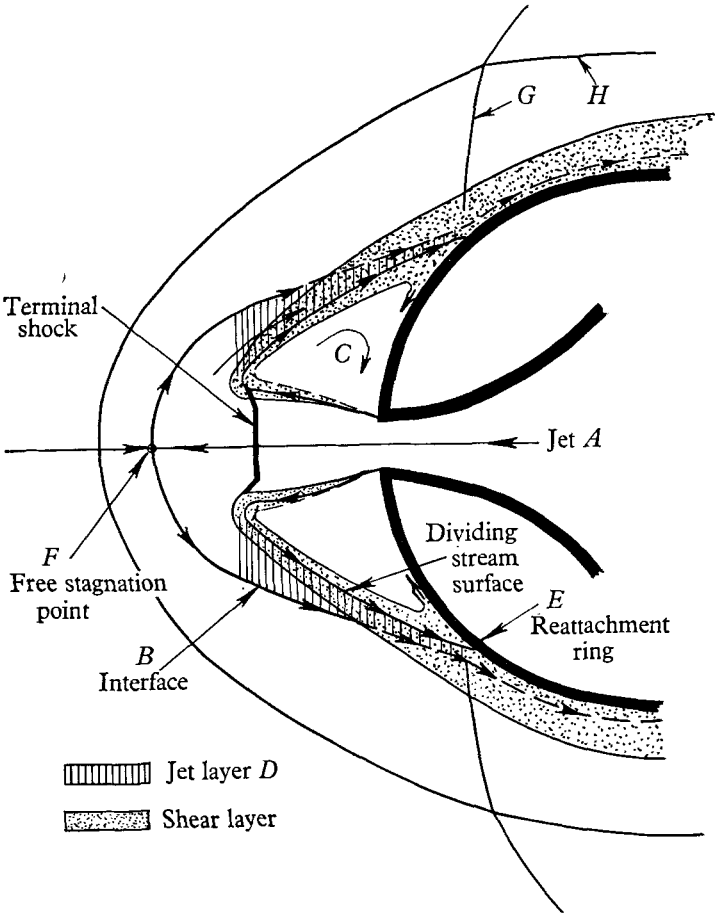

FIGURE 3. Features of the flow field.

dead-air region C around the jet. The fluid from the jet is deflected out and back over the dead-air region in the *jet layer*, to a *reattachment ring E*. The dividing stream surface springing from the orifice returns to the body surface at *E*, and a *shear layer* forms on either side of it. Fluid is entrained into the shear layer from the dead-air region and returned at the reattachment ring. The jet layer turns along the model surface at *E* and flows away downstream. The pressure rise

associated with the reattachment of the shear layer causes a *turning shock G* in the jet layer and the flow from the mainstream outside the interface. A *shear surface H* runs downstream from the intersection of the turning shock with the bow shock.

In a steady flow, both the free stream and the jet come to rest on the axis at a *free stagnation point F*, where the pressure is the free-stream Pitot pressure p_{0f}. The jet total pressure p_{0j} must be reduced to p_{0f} by some shock system in the jet, the structure of which will be examined later. p_{0j} cannot be less than p_{0f}, or there will be no outflow.

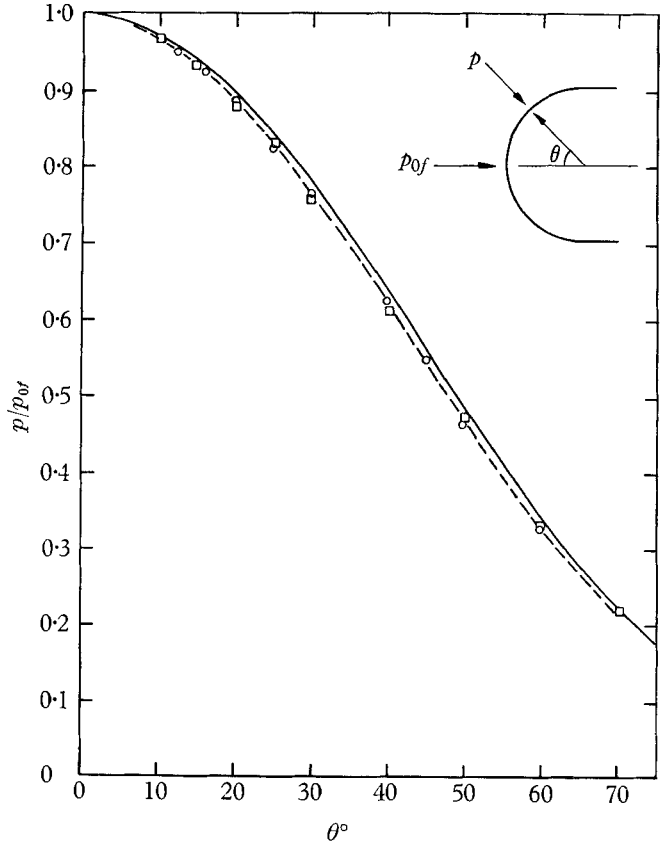

FIGURE 5. Static pressures recorded on 2 in. hemispherical models with no jet. $M_\infty = 2{\cdot}5$. ---, experiment; —, modified Newtonian theory.

As the jet total-pressure ratio $P(=p_{0j}/p_{0f})$ increases from its minimum value of 1, the bow shock moves forward and the pressure on the forepart of the body drops. In general this process is continuous except for a small critical range of P where the trend is reversed. Below the critical range the flow is observed to have more than one jet cell, and is generally unsteady. Above the critical range the flow is mainly steady with a single jet cell terminated by a normal shock. The change from one type of flow to the other is intermittent in character, the proportion of time for which a steady flow exists increasing as P increases. The estimated

value of P midway between the inception of the transition and its completion will be referred to as the critical value, P_{crit}, and is a function of jet size and nose shape. For the model shown in figure 4, plate 1, $P_{\text{crit}} = 1{\cdot}37$. The photographs show clearly the change in the nature of the flow.

A more detailed description of the flow field is presented by Sutton & Finley (1964).

5. Experimental results

Figure 5 shows the non-dimensional static-pressure distributions measured on the surface of the 2 in. diameter hemisphere-cylinders with no jet. Also shown is the pressure predicted by the modified Newtonian theory:

$$p/p_{0f} = \cos^2\theta + (p_\infty/p_{0f})\sin^2\theta.$$

This equation gives a good approximation to the observed pressure.

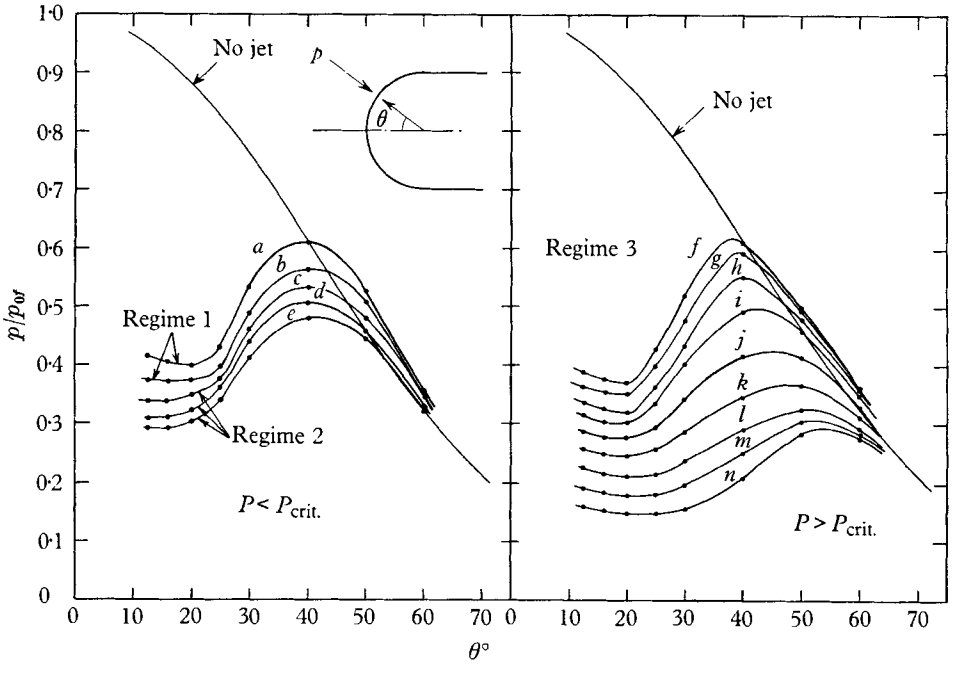

FIGURE 6. Static pressures recorded on 2 in. hemispherical model. $M_\infty = 2{\cdot}5$, $M_j = 1$, $\gamma = 1{\cdot}4$, $D = 7{\cdot}6$. Values of P: *a*, 1·05; *b*, 1·08; *c*, 1·15; *d*, 1·25; *e*, 1·35; *f*, 1·52; *g*, 1·68; *h*, 2·08; *i*, 2·23; *j*, 2·84; *k*, 3·73; *l*, 4·70; *m*, 5·50; *n*, 6·54.

Unless otherwise stated all results now presented refer to air jets leaving the orifice at $M_j = 1$.

The static pressures observed on the model shown in figure 4, plate 1, for which $\lambda = 1$, $D = 7{\cdot}6$, are given in figure 6. Figure 6(*a*) shows the values for $P < P_{\text{crit}}$, and figure 6(*b*) for $P > P_{\text{crit}}$. The curve determined with no jet is also shown. Near to the jet there is a low-pressure region corresponding to that part of the surface adjacent to the dead-air region (*C*, figure 3). As θ increases, p falls to a minimum value p_d, defined as the experimental *dead-air pressure*, and then

rises to a maximum p_m, at θ_m, near to the reattachment point.The reattachment is believed to occur just before the pressure maximum, therefore p_m will be called the *reattachment pressure* and θ_m the *reattachment angle*. At larger θ the static pressure tends to the value with no jet.

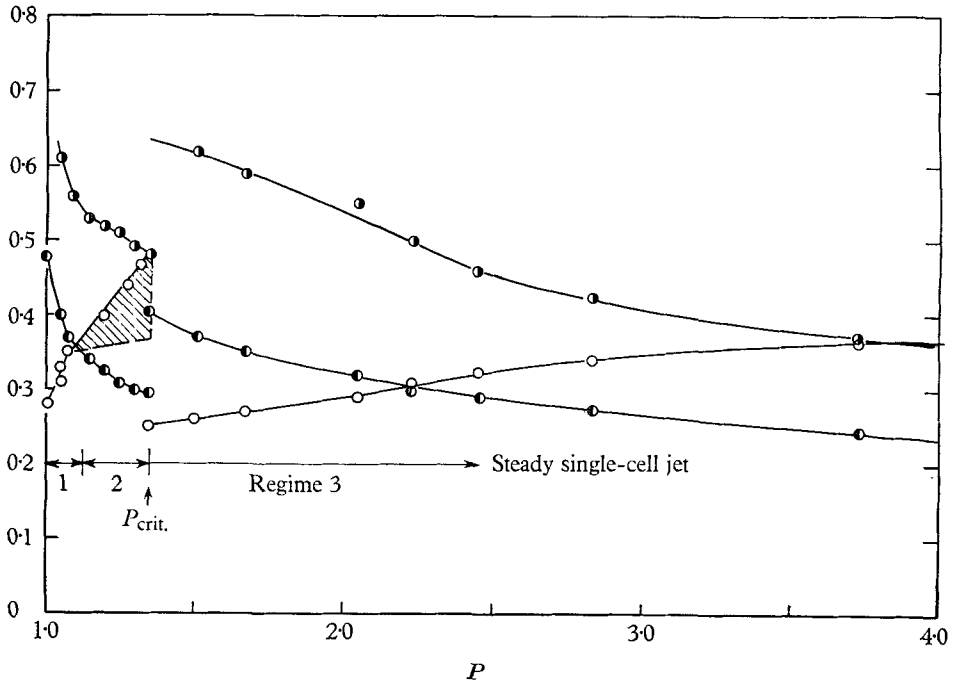

FIGURE 7. Variation of dead-air pressure p_d, reattachment pressure p_m, and bow-shock stand-off distance l_b, with jet total-pressure ratio. $M_\infty = 2{\cdot}5$, $M_j = 1$, $\gamma = 1{\cdot}4$, $D = 7{\cdot}6$, $\lambda = 1$. ◑, p_m/p_{0f}; ◐, p_d/p_{0f}; ○, l_b/d_m.

The general pressure level falls as P increases except through the critical range of P (compare figure 6(*a*), $P = 1{\cdot}35$, and figure 6(*b*), $P = 1{\cdot}52$). Figure 7 shows the dead-air pressure p_d, the reattachment pressure p_m, and the bow-shock stand-off distance l_b, measured from photographs, as functions of P. The discontinuity at P_{crit} is clearly visible. For $1 < P < 1{\cdot}13$, a steady flow with more than one jet cell was observed (figure 4(*a*)). This is referred to as regime 1. As P increases regime 1 breaks down, and an unsteady flow, regime 2, is observed in which all the features of the flow fluctuate considerably (figure 4(*b*) and (*c*)). A steady single-cell flow begins to appear for short periods when $P = 1{\cdot}35$, and is fully established when $P = 1{\cdot}42$. The steady flow with a single jet cell will be termed regime 3, and persists to the highest values of P attainable with the apparatus (figure 4(*d*), (*e*) and (*f*)).

Figure 8 shows the pressure distributions for a hemisphere-cylinder with a smaller jet ($D = 16{\cdot}4$). The same general features are to be observed, but the static pressure level for a given value of P is higher. For this model, $P_{\text{crit}} = 3{\cdot}0$. Photographs are shown in figure 9(*a*), (*b*), (*c*), plate 2. The flow in the neighbourhood of the reattachment (*E*, figure 3) fluctuates even when the jet is steady.

Regime 3 is divided into flows with slightly fluctuating reattachment, regime 3*a*, and those with effectively steady reattachment, regime 3*b*. The reattachment is deemed to be steady if a clear image of the shear surface H (figure 3) is found on a long exposure photograph of the flow. The shear surface is very thin, so that if the turning shock G (figure 3) fluctuates, no image of the shear surface is found except in spark photographs. Figure 9 (*b*), plate 2, shows regime 3*a* and 9 (*c*) shows regime 3*b*.

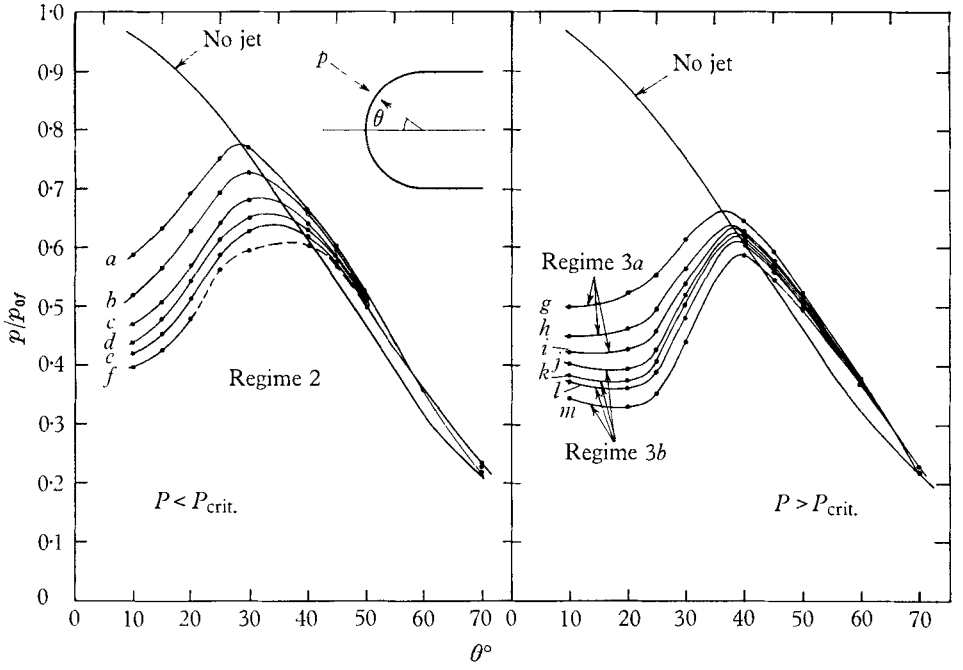

FIGURE 8. Static pressures recorded on 2 in. hemispherical model. $M_\infty = 2{\cdot}5, M_j = 1, \gamma = 1{\cdot}4$, $D = 16{\cdot}4$. Values of P: *a*, 1·26; *b*, 1·51; *c*, 1·79; *d*, 2·07; *e*, 2·30; *f*, 2·55; *g*, 3·25; *h*, 4·25; *i*, 4·75; *j*, 5·25; *k*, 5·75; *l*, 6·25; *m*. 7·25.

The pressures measured in regime 3 on a hemisphere-cylinder for which $D = 33{\cdot}3$ are shown in figure 10, which also shows values for a jet which is supersonic in the exit plane. The results for $M_j = 2{\cdot}6$, $D = 9{\cdot}4$, are of the same kind as those for $M_j = 1$. The critical total-pressure ratio P_{crit} was 10·4 in this case.

Pressure measurements were made with carbon dioxide replacing air in the jets from convergent nozzles, and no significant differences were observed, either in static pressure, or in the value of P_{crit}.

Figures 9 (*d*), (*e*) and (*f*) show that the flow about other spheroidal noses is of the same type. A continuous record of the static pressure at a point near the jet was made for each model. Some of these records are shown to a common scale in figure 11. The curves for $\lambda = 1$ are plotted from figures 6, 8, 10 and refer to the minimum or dead-air pressure p_d. The curves for $\lambda = 0$ and 0·5 were recorded electrically from a single point which may not have been quite at the pressure minimum. The tapping on the 1 in. diameter models for $\lambda = 1$, $\lambda = 2$ was far from the minimum, so curves for these models are not presented.

The discontinuity in p_d between either regime 1 or 2 and regime 3 is clearly visible, and values of P_{crit} from these records and those for $\lambda = 1$, $\lambda = 2$, are shown in figure 12 as a function of D and λ. The approximately linear variation of P_{crit} with D for values of $P_{\text{crit}} < 5$ is notable.

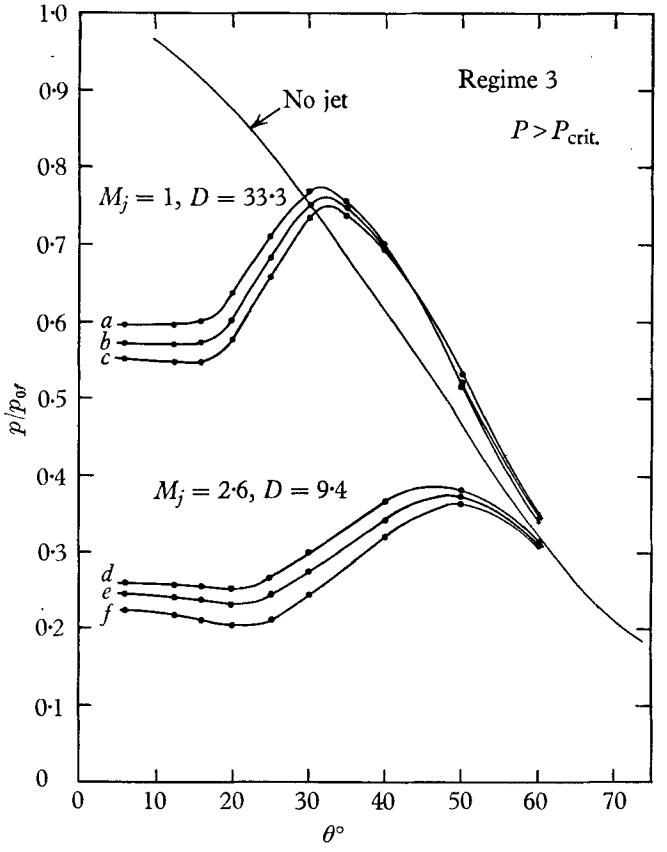

FIGURE 10. Static pressures recorded on 2 in. hemispherical models. Values of P: *a*, 6·75; *b*, 8·45; *c*, 9·75; *d*, 10·7; *e*, 12·0; *f*, 13·3.

In figure 11 (*a*), the maximum observed values of p_d in regime 3 can be seen to lie in a narrow band. Some of the irregularities of the curves in regime 3 can be related to changes in the reattachment flow. In particular, the change from regime 3*a* to regime 3*b* for the two cases $\lambda = 1$, $D = 16{\cdot}4$, and $\lambda = 0{\cdot}5$, $D = 10{\cdot}2$, near $P = 5$ is marked.

Other quantities connected with the flow were measured from the schlieren photographs. Figure 7 gives the bow-shock stand-off distance l_b for the model ($\lambda = 1$, $D = 7{\cdot}6$). The interface is not generally visible in a photograph, as, when $T = 1$, there is no discontinuity of density or density gradient across it. At high mass flow rates, however, there was a slight difference between $T_{0\infty}$ and T_{0j}, and an image of the interface, nearly spherical, may be seen in figures 4 (*f*), plate 1, and 9 (*f*), plate 2.

An indirect method was adopted to locate the interface in other photographs.

The co-ordinates of the bow shock were matched by the method of least squares to general symmetrical conic sections. Van Dyke & Gordon (1959) have calculated the bodies which support shocks of conic meridian section, and which are themselves closely conic sections. The solution gives the diameter d_f of the tangent sphere to the interface nose, the fineness λ of the interface, and the

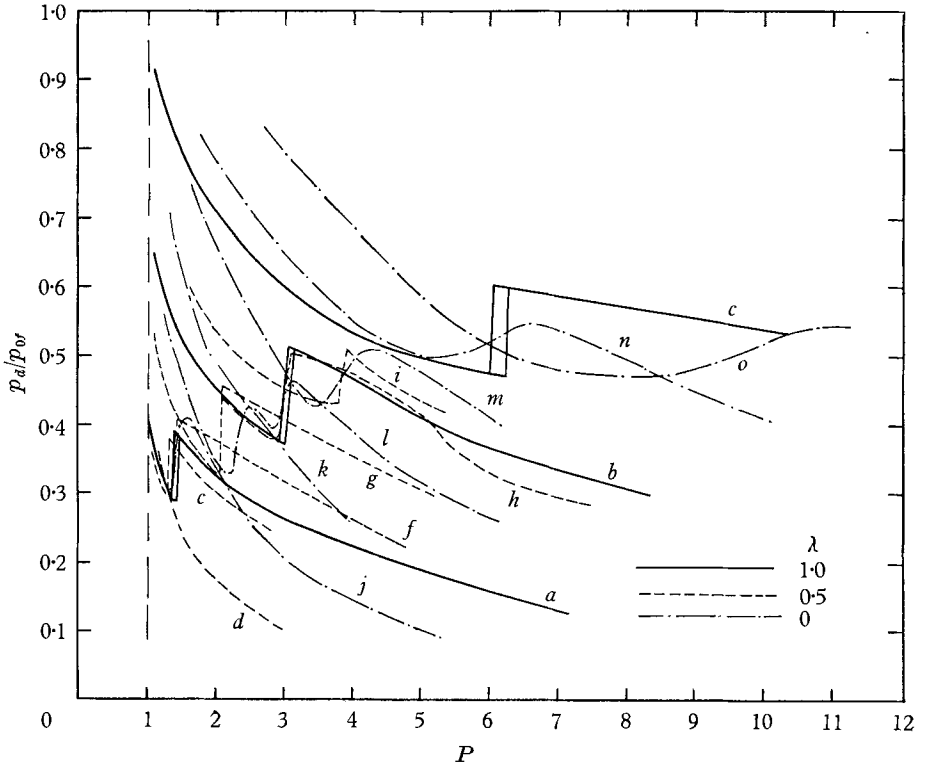

FIGURE 11. Variation of dead-air pressure p_d with jet total-pressure ratio P as recorded on various spheroidal models. $M_\infty = 2{\cdot}5$, $M_j = 1$, $\gamma = 1{\cdot}4$. ——, $\lambda = 1$ with values of D: *a*, 7·6; *b*, 16·4; *c*, 33·3. – – –, $\lambda = 0{\cdot}5$ with values of D: *d*, 3·8; *e*, 5·29; *f*, 6·25; *g*, 7·70; *h*, 10·2; *i*, 14·3. —·—, $\lambda = 0$ with values of D: *j*, 3·97; *k*, 5·21; *l*, 6·25; *m*, 7·9; *n*, 10·2; *o*, 14·3.

separation of the bow shock from the interface $(l_b - l_f)$. Since the bow shock is not exactly a conic, an unavoidable uncertainty appears in the results. This is small in the calculation of d_f, and when the calculated value could be checked, as in figures 4(*f*), plate 1, and 9(*f*), plate 2, no significant discrepancies were found.

The interface nose was calculated to be slightly blunter than a sphere. The average result is $\lambda \simeq 0{\cdot}9$, but the difference between $\lambda = 0{\cdot}9$ and $\lambda = 1$ is less than the standard deviation of the determination, which was about 0·4. The interface will therefore be treated as spherically nosed hereafter.

The results calculated from the photographs are presented in connexion with the analysis later.

6. Analysis of steady flows

6.1. *Conditions on the flow model*

The flow, as sketched in figure 3, is divided into regions within which simplifying assumptions are made. The interactions of these regions with one another give the framework of the analysis.

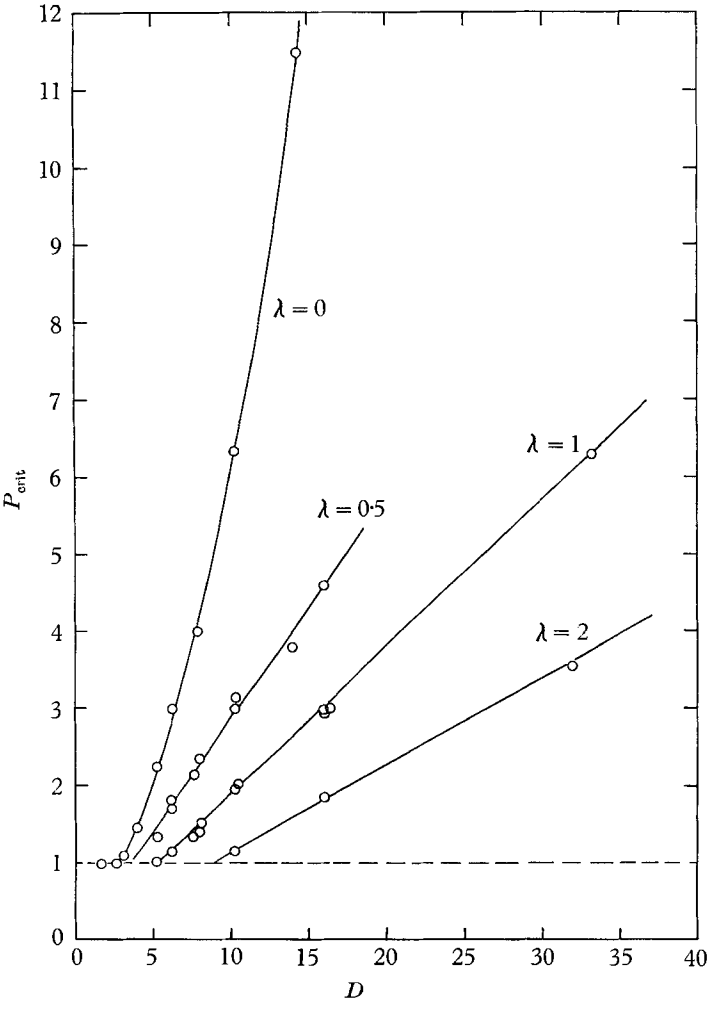

FIGURE 12. Variation of the critical total-pressure ratio P_{crit} for models of various shapes with relative body size D. $M_\infty = 2{\cdot}5$, $M_j = 1$.

The pressure in the dead-air region C, figure 3, is taken to be effectively uniform, the *dead-air pressure* p_d. The initial development of the jet is taken to be that of a free jet of total pressure p_{0j} exhausting to a still atmosphere of pressure p_d. A condition imposed on this *equivalent free jet* is that its total pressure p_{0j} fall to p_{0f} at the free stagnation point. The final shock of the jet structure, the terminal shock, must be a normal shock.

The free-stream Mach number is taken to be sufficiently high for the pressure on the interface to be given by modified Newtonian theory. The jet layer outside the dead-air region is assumed thin, and since the pressure p_d within the dead-air region is uniform, matching p_d to the pressure on the outside of the jet layer gives a conical interface.

In front of the dead-air region, the interface is smoothly curved, crossing the axis normally, and the pressure is high, as is required to turn the jet out into the jet layer. The pressure forces on the interface must be balanced by the pressure forces and momentum fluxes of the jet and jet layer and the force exerted on the dead-air region by the nose.

The shear layer on either side of the dividing stream surface reattaches to the body at E (figure 3). The flow near the reattachment ring must be such as to make good the entrainment into the shear layer from the dead-air region. The mechanism of reattachment is discussed in detail by Chapman *et al.* (1957), Cooke (1963) and others. The Chapman model has been used to guide an independent experimental study of an annular shear layer attaching to a hemisphere by Finley (1963). This showed that the jet layer would turn through a deflexion angle ϵ in the range $8° < \epsilon < 22°$ on encountering the body surface.

The jet must be of such length that it can support an interface which meets the body surface at an appropriate value of ϵ.

6.2. *Momentum balance for the interface*

The interface is taken to be a spherically blunted cone as shown in figure 13. It is specified by the cone semi-apex angle α and the diameter of the blunting sphere d_f. If ϕ is the local inclination of the surface to the free stream, and p_∞ the free-stream static pressure, modified Newtonian theory gives

$$p/p_{0f} = \sin^2\phi + (p_\infty/p_{0f})\cos^2\phi.$$

The dead-air pressure p_d is therefore given by

$$p_d/p_{0f} = \sin^2\alpha + (p_\infty/p_{0f})\cos^2\alpha. \tag{1}$$

Figure 13 shows the control surface for the force and momentum balance as a broken line. The interface is closed by a surface, including the jet orifice plane, which meets the interface in the conical region. The pressure on this surface is constant, the dead-air pressure p_d, except over the jet orifice where it is p_j. The pressure on the interface is integrated to give the momentum-balance equation

$$\tfrac{1}{8}\pi d_f^2\cos^4\alpha(p_{0f}-p_\infty) - \tfrac{1}{4}\pi d_j^2(p_j-p_d) = w_j v_j + w_l v_l\cos\alpha, \tag{2}$$

where w_j and v_j are respectively the jet mass flow and exit-plane velocity, w_l and v_l are the jet-layer mass flow and velocity leaving the control surface. The total momentum of the flow in the jet layer is assumed to be that of the jet mass flow expanded uniformly and isentropically from p_{0f} to p_d; the non-uniformity of total pressure due to the shock structure in the jet is neglected.

A specific flow-force function G, a mass-flow function W and a velocity function

V are introduced, with suffices j when used for the jet and l for the jet layer, where

$$\left.\begin{aligned} G &= (pA+wv)/w(C_p T_0)^{\frac{1}{2}} = G(M,\gamma),\\ W &= w(C_p T_0)^{\frac{1}{2}}/Ap_0 = W(M,\gamma),\\ V &= v/(C_p T_0)^{\frac{1}{2}} = V(M,\gamma). \end{aligned}\right\} \tag{3}$$

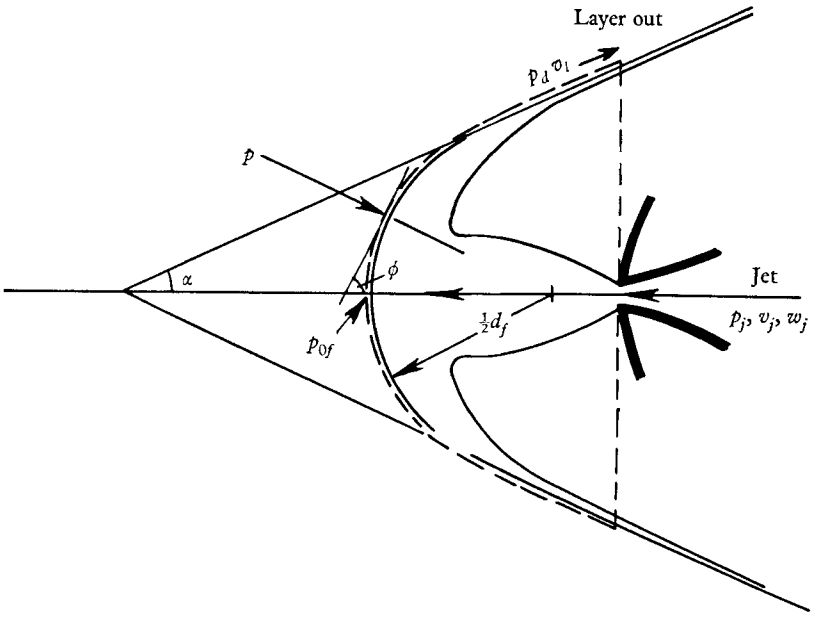

FIGURE 13. Control surface used for the momentum balance of § 6.2.

The product GW is denoted by I. If the jet flow force† F_j is defined by

$$F_j = \tfrac{1}{4}\pi d_j^2 p_j + w_j v_j, \tag{4}$$

then

$$F_j = G_j W_j / \tfrac{1}{4}\pi d_j^2 p_{0j} = I_j \tfrac{1}{4}\pi d_j^2 p_{0j}. \tag{5}$$

Equation (2) may now be written

$$D_f^2 = PI_j\{1 + (V_l/G_j)\cos\alpha\}Z^{-1} - (p_d/p_{0f})Z^{-1}, \tag{6}$$

where $D_f = d_f/d_j$ and $Z = \frac{1}{2}\cos^4\alpha(1 - p_\infty/p_{0f})$, a function mainly of p_d/p_{0f}.

The relation between p_d/p_{0f} and P/D_f^2 for the case $M_\infty = 2{\cdot}5$, $M_j = 1$, $\gamma = 1{\cdot}4$, has been calculated from equation (6), and is shown in figure 14. It can be seen that if $P > 5$, the second term on the right of equation (6) may be neglected. Physically this is to say that p_d acting on the area of the jet is negligible as compared to the other pressure forces.

Now $d_f/d_m = (d_f/d_j)(d_j/d_m)$ so that, when P is large, equation (6) may be written

$$(d_f/d_m)^2 = (PI/D^2)\{1 + (V_l/G_j)\cos\alpha\}Z^{-1}.$$

† The quantity $F(= pA + wv)$ appears frequently in fluid mechanics. Benjamin (1962) has suggested the name 'flow force' as preferable to the commonly met 'impulse'.

The jet flow-force coefficient C_F, which is the jet force made non-dimensional with respect to p_{0f} and the cross-section area of the body, and so defined by

$$C_F = F_j/\tfrac{1}{4}\pi d_m^2 p_{0f} = PI/D^2, \tag{7}$$

is now introduced. Equation (6) becomes

$$(d_f/d_m)^2 = C_F\{1 + (V_l/G_j)\cos\alpha\}Z^{-1}. \tag{8}$$

At high values of M_∞, Z tends to a function of α only.

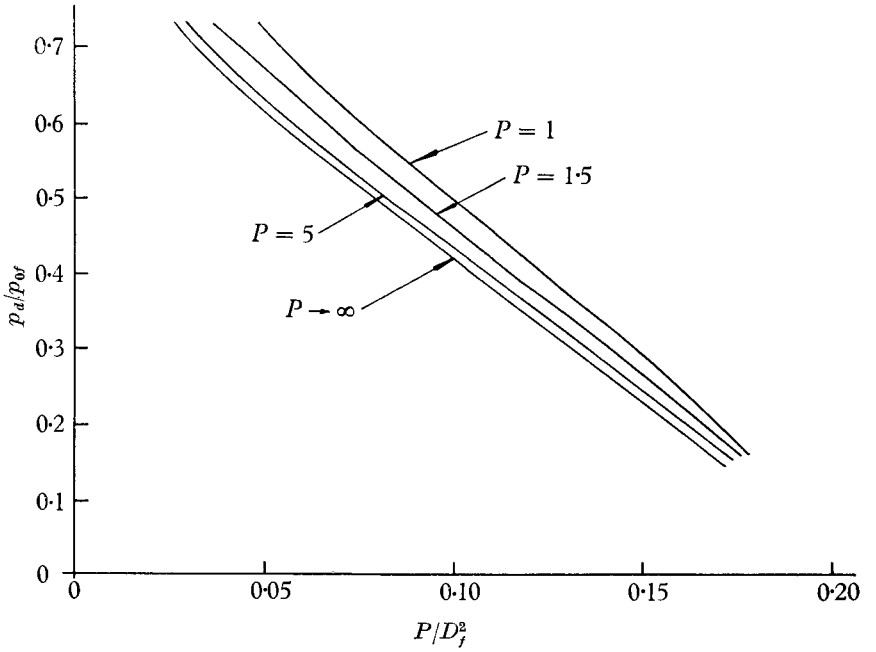

FIGURE 14. Relation between dead-air pressure p_d and the interface-blunting-sphere diameter calculated from equation (6). $M_\infty = 2{\cdot}5$, $M_j = 1$, $\gamma = 1{\cdot}4$.

V_l/G_j depends on α and on M_j and γ_j. If the dependence on M_j and γ_j can be neglected, equation (8) gives a single relation between d_f/d_m and α for any given value of C_F. The variation of V_l/G_j with γ_j and M_j is shown in tables 1, 2 for the case $p_d/p_{0f} = 0{\cdot}314$.

Table 1 shows that γ_j may vary without any significant change in the relation between d_f/d_m and α, and also that, since I_j does not vary much with γ_j, C_F is approximately proportional to P at constant M_j. Table 2 shows that for the relation between d_f/d_m and α to remain unaltered, C_F need only increase by approximately 5 % as M_j varies from 1 to 3. I_j, however, varies widely, so that C_F is not proportional to P.

Thus equation (8) shows that

$$d_f/d_m = f_1(C_F, \alpha) \tag{9}$$

with small and calculable changes in the relation depending on M_j, and γ_j, so long as P is high and M_∞ is high enough for p_∞/p_{0f} to be small compared to l. This will be assumed during the rest of the analysis.

6.3. *The distance of the interface from the body*

The jet of a steady flow of regime 3 is terminated by a single normal shock crossing the axis, as in figure 4(*d*), (*e*) and (*f*), at a distance l_s from the orifice. The total-pressure ratio across this shock P determines the Mach number M_s of the flow entering it. Within the shock structure of the first cell, the flow of all jets

γ_j	1·33	1·40	1·67
V_l/G_j	0·76	0·76	0·74
I_j	1·26	1·27	1·33

TABLE 1. $M_j = 1$, $p_d/p_{0f} = 0{\cdot}314$.

M_j	1	1·5	2	2·5	3
V_l/G_j	0·76	0·72	0·68	0·64	0·61
I_j	1·27	1·13	0·84	0·57	0·37

TABLE 2. $\gamma = 1{\cdot}4$, $p_d/p_{0f} = 0{\cdot}314$.

of given M_j, γ_j is similar. In particular the variation of Mach number along the axis is prescribed by and depends only on M_j and γ_j. The value of P therefore determines also the position at which the normal shock crosses the axis.

The Mach-number distribution along the axis can be calculated theoretically. Owen & Thornhill (1952) give a solution by the method of characteristics for a jet with $M_j = 1{\cdot}0038$ and $\gamma_j = 1{\cdot}4$ expanding into a vacuum. That solution has been used here for jets with $M_j = 1$ and $\gamma_j = 1{\cdot}4$. For other values of M_j and γ_j the approximate methods of calculation suggested by Adamson & Nicholls (1959) have been used.

Matching the Mach number M_s upstream of the shock as a function of P with Owen & Thornhill's solution shows that, when $P > 5$,

$$L_s = l_s/d_j = 0{\cdot}77P^{\frac{1}{2}} \tag{10}$$

very closely for $M_j = 1$ and $\gamma_j = 1{\cdot}4$. Since $C_F = PI/D^2$, equation (10) can be written

$$l_s/d_m = 0{\cdot}68C_F^{\frac{1}{2}}. \tag{11}$$

Similar relations apply for other values of M_j, so that l_s/d_m is a function of M_j, γ_j and C_F.

A model of the jet and interface flow is sketched in figure 15. The jet is taken to develop as an equivalent free jet, exhausting from p_{0j} to p_d, but is assumed to terminate on a plane through the point at which the terminal shock crosses the axis. The diameter d_s of the jet in this plane may be obtained from the data presented by Love *et al.* (1959). For $M_j = 1$, the data may be represented closely by the equation

$$D_s^2 = (d_s/d_j)^2 = 0{\cdot}3 + 0{\cdot}325P.(p_d/p_{0f})^{-1}, \tag{12}$$

so that at constant or very high M_∞, (d_s/d_m) is a function of C_F, α, and M_j, γ_j.

The fluid leaving the jet in the plane of the terminal shock is assumed to be uniform, with total pressure p_{0f}. It is assumed to be choked in an annulus of

width δ running from the edge of the jet to the interface as shown in figure 15. As in the approximate bluff-body solutions of Love (1957), the flow in this annulus is assumed uniform in the direction of the tangent to the interface. The mean diameter of the annulus is taken to be approximately d_s. The equation of continuity then gives, for $M_j = 1$,

$$\pi d_s \delta p_{0f} = \tfrac{1}{4}\pi d_j^2 p_{0j},$$

or
$$\Delta = \delta/d_j = P/4D_s, \tag{13}$$

or
$$\delta/d_m = (PI/D^2).I^{-1}.(d_s/d_m)^{-1}, \tag{14}$$

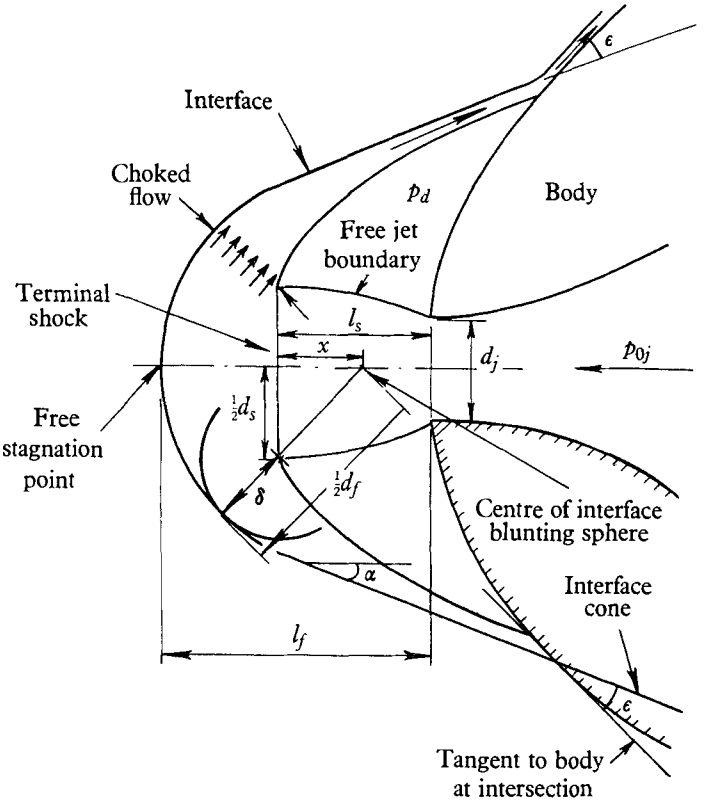

FIGURE 15. Flow model used to determine the position of the interface.

showing that δ/d_m is a function of C_F, α, and M_j, γ_j (since for other M_j the 4 in (13) would be replaced by a different numerical constant).

The distance x in figure 15 is given by Pythagoras's theorem. If $X = x/d_j$, then

$$4X^2 = (D_f - 2\Delta)^2 - D_s^2, \tag{15}$$

and all these quantities are functions of C_F, α, M_j and γ_j.

If l_f is the distance from the jet orifice to the point where the interface crosses the axis,

$$l_f/d_m = (l_s/d_m) + (d_f/2d_m) - (x/d_m), \tag{16}$$

so that the interface position is a function of C_F, α, M_j and γ_j.

6.4. *Matching the interface to the body*

If a shear layer reattaches to a solid surface, the flow immediately outside it is deflected through an angle ϵ. This angle, as predicted by the reattachment model of Chapman *et al.* (1957) is a function of the Mach number of the flow just outside the shear layer and the velocity profile of the layer. With the assumptions already made for this flow, ϵ would be a function of p_d/p_{0f} only. The jet-layer initial total pressure is not uniformly p_{0f}, however, so that ϵ is found to depend on other variables, too, but the magnitude of such effects will be shown to be small.

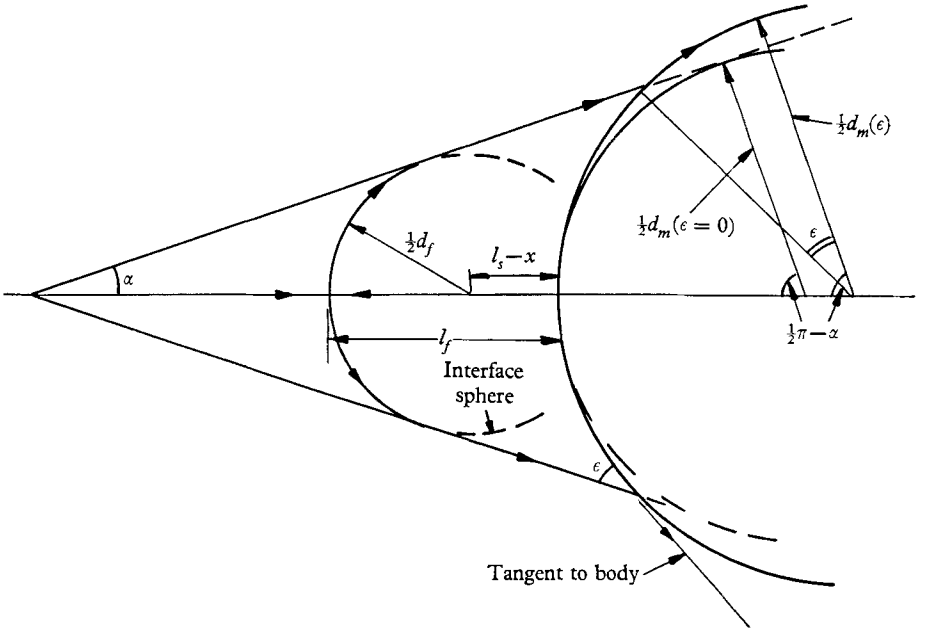

FIGURE 16. Geometry of the interface and a spheroidal body.

If the body nose is smoothly curved, as in figures 15 and 16 which show a sphere, and the jet layer near reattachment is thin, then if ϵ is fixed or a function of α, a specification of α will fix the position of the interface cone. Then for any value of l_f/d_m there is only one value of d_f/d_m such that the interface-blunting sphere is tangent to the cone. The non-dimensional distance l_f/d_m to the interface is a function of $(C_F, \alpha, M_j, \gamma_j)$ as shown in equations (10) to (16). The non-dimensional diameter d_f/d_m of the blunting sphere determined from the length of the jet, $f_2(C_F, \alpha, M_j, \gamma_j)$ must equal d_f/d_m determined from the momentum balance of § 6.2, $f_1(C_F, \alpha, M_j, \gamma_j)$.

$$f_1(C_F, \alpha, M_j, \gamma_j) = (d_f/d_m) = f_2(C_F, \alpha, M_j, \gamma_j).$$

Therefore (provided P and M_∞ are high enough)

$$\alpha = f_3(C_F, M_j, \gamma_j), \tag{17}$$

and, since f_1, f_2 vary little with γ_j, α is effectively a function of C_F and M_j only; and so, within the assumptions made, are all the other dependent variables of the flow.

The flow model may be used to derive p_d/p_{0f} explicitly as a function of M_j, C_F. From the geometry of figure 16, when $\epsilon = 0$, for a spherically nosed body

$$(d_m/d_f) = (\tfrac{1}{2}d_f \sin\alpha + \tfrac{1}{2}d_m + l_s - x)/\tfrac{1}{2}d_f \sin\alpha,$$

so that, when ϵ is zero,

$$D_{(\epsilon=0)} = \{D_f + 2\sin\alpha(L_s - X)\}/(1-\sin\alpha), \tag{18}$$

and, when ϵ is not zero,

$$D = D_{(\epsilon=0)}(1-\sin\alpha)/(\cos\epsilon - \sin\alpha),$$

giving

$$D = \{D_f + 2\sin\alpha(L_s - X)\}/(\cos\epsilon - \sin\alpha). \tag{19}$$

If α, P are treated as independent variables for calculation, D_f, L_s, X may be found from equations (6), (10) (or exactly from Owen & Thornhill 1952), (12), (13) and (15). Equation (19) is then used with equation (1) to give p_d/p_{0f} as a function of C_F, M_j, and ϵ for the flow about a hemisphere. In calculation it is not necessary to limit work to the case of high P and M_∞.

The relations of equations (18), (19) are essentially geometric, and a plane projection may be applied to figure 16 to give the geometry of interfaces meeting spheroids other than hemispheres. Equivalent bodies must pass through a given orifice and meet a given interface at the same angle.

The projection is applied to the case $\epsilon = 0$ for simplicity, and it is assumed that the relation between equivalent bodies is not critically dependent on the value of ϵ. Then, if D_E is the value of D for a spherical body equivalent to a spheroidal body given by D, λ,

$$D_E/D = \{\lambda - (\lambda^2 + \cot^2\alpha)^{\frac{1}{2}}\}/(1 - \operatorname{cosec}\alpha). \tag{20}$$

The effect of a non-zero value of ϵ on the relation of equation (20) increases with λ. The fit of a square-ended body to a given interface is independent of ϵ, whilst the effect for a sphere is given by comparing equations (18) and (19). A non-spheroidal body may be assigned an approximate value of λ.

6.5. *Application of the analysis*

The functional relationship of equation (17) may be used to correlate experimental data. Figure 17 shows for regime 3 the dead-air pressure $p_{\bar{d}}$, the reattachment pressure p_m and the reattachment angle θ_m obtained from figures 6, 8 and 10, plotted against $C_F^{\frac{1}{2}}$. The results collapse well to single curves when it is considered that the values of P start at 1·52 ($D = 7{\cdot}6$). Figure 18 shows data obtained from photographs, and the relation of equation (11) for l_s/d_m. The values of l_s approach this line closely when $P > 4$. The bow-shock stand-off distance l_b appears to be linearly related to $C_F^{\frac{1}{2}}$, and if the values are extrapolated to $C_F = 0$ they include the case with no jet. The distance to the interface l_f is also shown as calculated from the bow-shock co-ordinates. These results show that the relationship of equation (17) adequately describes the flow.

Figure 19 shows p_d/p_{0f} from figure 11 plotted against $C_F^{\frac{1}{2}}$. To a large extent, the records for each nose shape come together. The tapping in the blunt ellipsoidal model ($\lambda = 0{\cdot}5$) was near the reattachment zone, and so shows greater

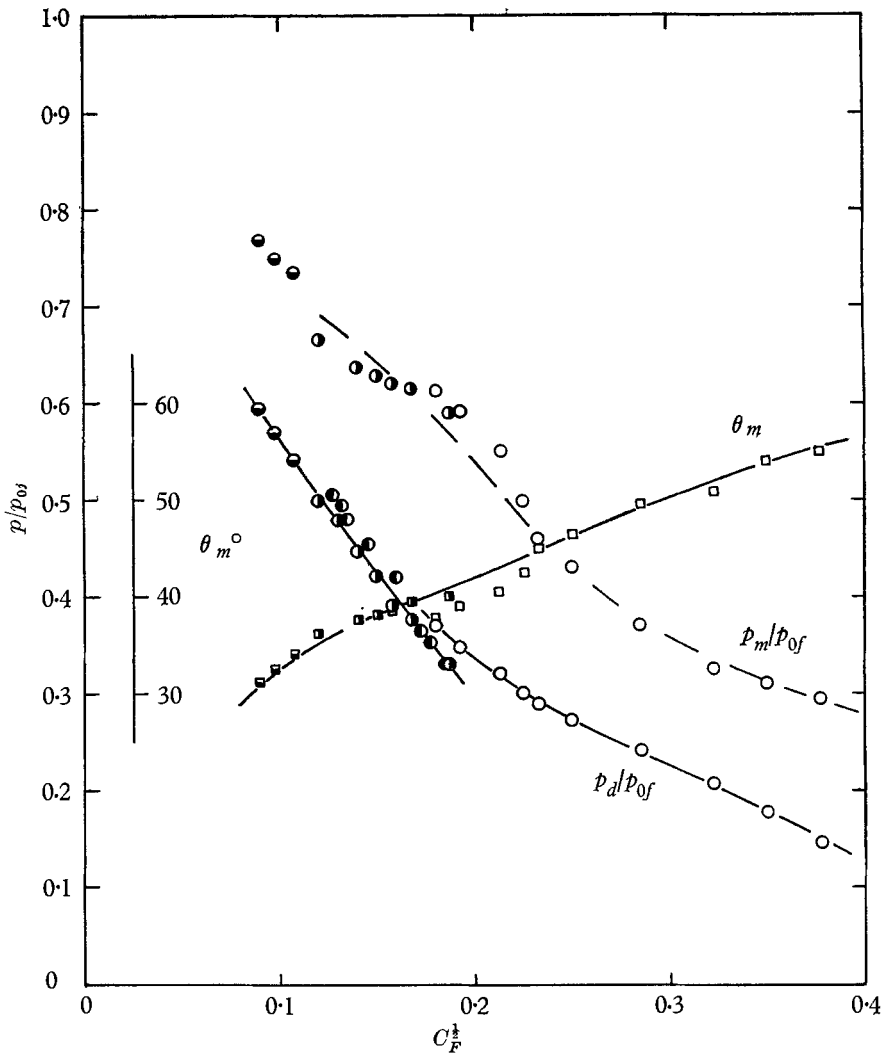

FIGURE 17. Experimental values of dead-air pressure p_d, reattachment pressure p_m, and reattachment angle θ_m, related to the jet flow-force coefficient C_F. $M_\infty = 2{\cdot}5$, $M_j = 1$, $\gamma = 1{\cdot}4$, $\lambda = 1$. ○, □, $D = 7{\cdot}6$; ◐, ◑, ◨, $D = 16{\cdot}4$; ◒, ⬓, $D = 33{\cdot}3$.

variations than those recorded for $\lambda = 0$. In some cases these can be related to changes in the reattachment flow.

The geometric relationship between body and interface used to derive D_E in equation (20) suggests that these results may be further brought together by relating them to an equivalent jet-flow-force coefficient C_{FE} defined by

$$C_{FE} = PI/D_E^2. \tag{21}$$

The ranges of p_d/p_{0f} covered by the curves in figure 19 are replotted against $C_{FE}^{\frac{1}{2}}$ in figure 20, and come together well. p_d/p_{0f} tends to be lower for higher values of λ, and this trend can be related to the turning at reattachment.

Figure 21 shows curves of p_d/p_{0f} calculated from the analytical model for the

case $M_\infty = 2{\cdot}5$, $M_j = 1$, $\gamma_j = 1{\cdot}4$, $\lambda = 1$, with $\epsilon = 0°$, $10°$, $20°$. The curve for $\epsilon = 0$ corresponds also to the predicted relationship between p_d/p_{0f} and C_{FE} for $\lambda = 0$, regardless of the value of ϵ. The subsidiary study of reattachment (Finley 1963) leads to an estimate for the value of ϵ which varies from approximately $10°$ at

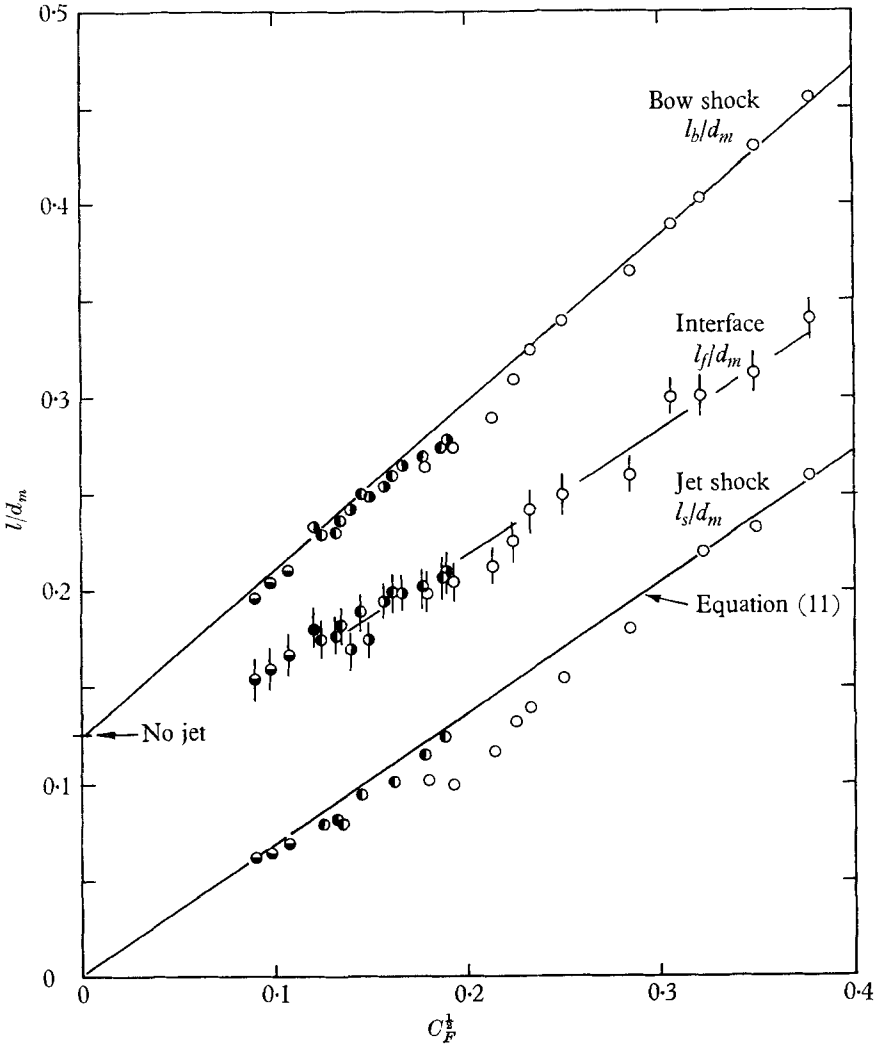

FIGURE 18. Bow shock (l_b), jet shock (l_s), and interface (l_f), positions as measured from photographs, related to the jet flow-force coefficient C_F. $M_\infty = 2{\cdot}5$, $M_j = 1$, $\gamma = 1{\cdot}4$, $\lambda = 1$. ○, $D = 7{\cdot}6$; ◐, ◑, $D = 16{\cdot}4$; ◒, $D = 33{\cdot}3$.

$C_F^{\frac{1}{2}} = 0{\cdot}1$ to approximately $20°$ at $C_F^{\frac{1}{2}} = 0{\cdot}3$. The experimental values of p_d/p_{0f} are shown for $\lambda = 1$ and $\lambda = 0$. They agree well, considering the assumptions made, but tend to diverge at high values of C_F. Figure 22 shows the calculated value of p_d/p_{0f} for $\lambda = 1$, $M_j = 2{\cdot}6$, together with the experimental values. Again agreement is good.

Figure 23 shows the predicted and experimental values of the distance to the interface. The analysis is seen to overestimate l_f at high C_F, and underestimate at

low C_F. It can be shown that making an allowance in the analysis for the jet-layer thickness (which is about $0{\cdot}4C_F d_m$ when $M_j = 1$ and $M_\infty = 2{\cdot}5$) brings the curves into closer agreement at high C_F. The remaining discrepancy at high C_F can be accounted for by the observation that the jet terminal shock becomes domed, not flat as assumed in the analysis. At low C_F the assumption of choked flow in the annulus δ underestimates l_f, since p_d/p_{0f} is above the critical pressure ratio.

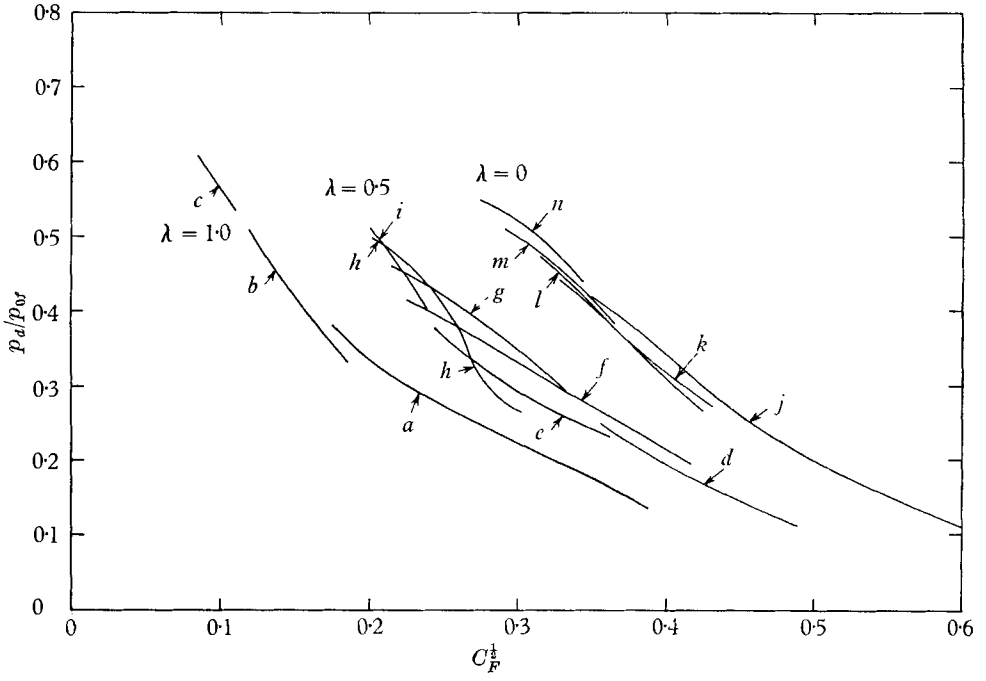

FIGURE 19. Experimental values of the dead-air pressure p_d on various spheroidal models (from figure 11) related to the flow-force coefficient C_F. $M_\infty = 2{\cdot}5$, $M_j = 1$, $\gamma = 1{\cdot}4$. Identification as in figure 11.

Many theoretical or empirical refinements may be introduced if it is desired to improve the numerical accuracy of the analysis, but the simple model predicts the main features and trends of steady flows with considerable success.

7. The structure and steadiness of the jet

The form of the jet must be consistent with the static pressure surrounding it, and with the fact that the total pressure on the axis must be reduced from p_{0j} to p_{0f}.

This condition will be assumed not to affect the initial development of the jet which will be taken to be the same as that of an *equivalent free jet* of total pressure p_{0j} exhausting to a still atmosphere of pressure p_d.

Such a free jet displays the well known series of jet cells described, for example, by Hartmann & Lazarus (1941). Figure 24 shows typical forms of the structure of an underexpanded jet, i.e. one in which the static pressure in the nozzle exit plane p_j is greater than the ambient pressure. The flow expands on leaving the

orifice, and the expansions are reflected by the free jet boundary as concurrent compression waves, which coalesce to form an *intercepting shock*. This shock is reflected at the axis either by a *regular reflexion* as in figure 24(*a*), for low pressure ratios p_j/p_d, or by forming a *Mach disc* as in figure 24(*b*) for high p_j/p_d. The

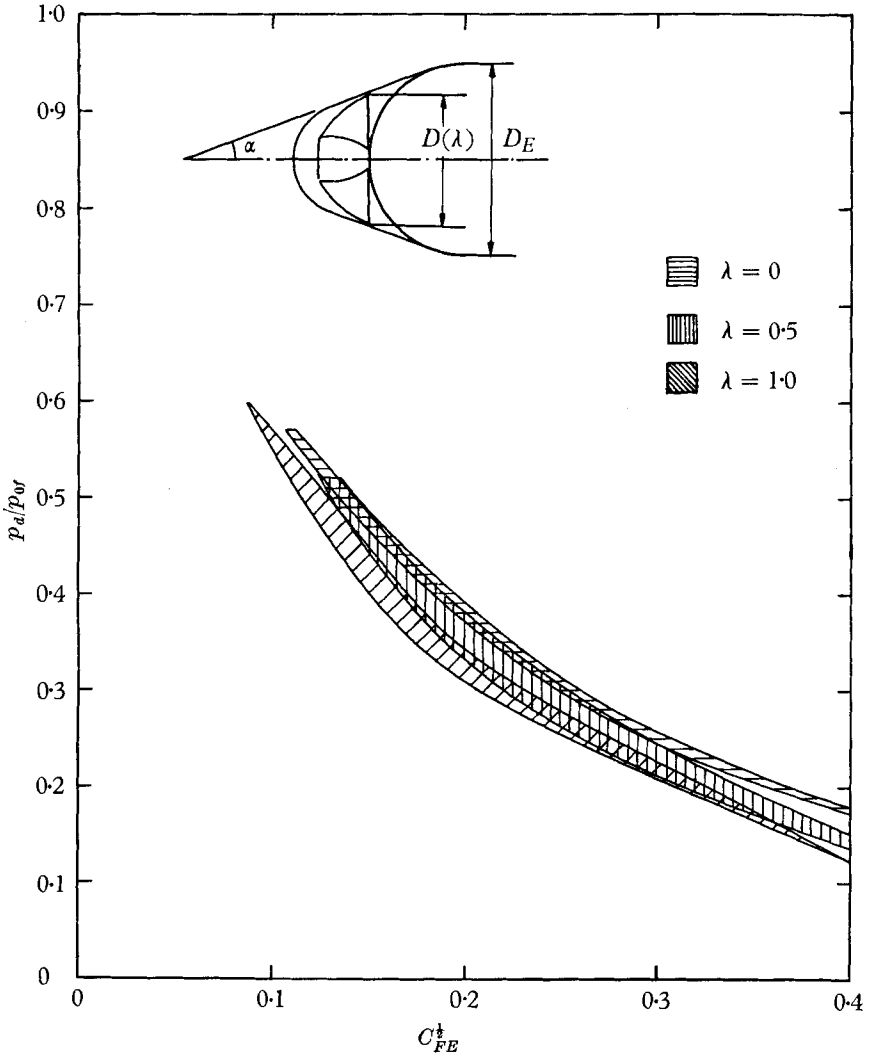

FIGURE 20. Dead-air pressure p_d for spheroidal models correlated to the equivalent jet-flow force coefficient C_{FE} based on the diameter of an equivalent spherical body.

reflexion at the axis ends the first cell of the jet, but further cells may be formed by repeated expansion and recompression of the jets.

Apart from any effects of viscosity, the initial flow depends on the exit Mach number M_j, the gas specific-heat ratio γ_j, and the exit static-pressure ratio p_j/p_d. The flow within the part of the first cell bounded by intercepting shock and Mach disc is independent of the static-pressure ratio p_j/p_d. This region is identically the same in the free jet and in the particular case of steady flow with

a single jet cell against a supersonic stream, described in § 6.3, except that the jet opposing a free stream is cut short by the terminal shock. The position of the intercepting shock is determined by p_j/p_d as well as M_j and γ_j in both cases. In the first cell of the free jet the position of the reflexion of the intercepting shock,

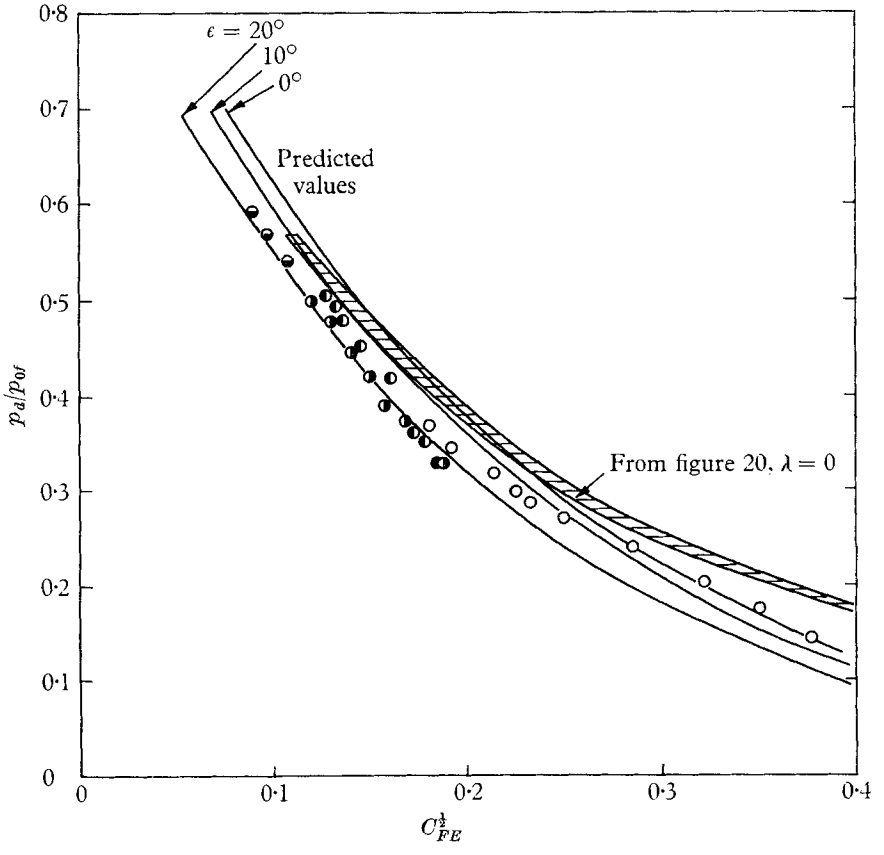

FIGURE 21. Dead-air pressure predicted by the flow model of § 6 compared with experimental values. $M_\infty = 2{\cdot}5$, $M_j = 1$, $\gamma = 1{\cdot}4$. Experimental values for $\lambda = 1$: ○, $D = 7{\cdot}6$; ◐, ◑, $D = 16{\cdot}4$; ◒, $D = 33{\cdot}3$.

and the development of the entire flow downstream of it, also depends on p_j/p_d. If l_w is the distance to the first shock wave crossing the axis of the free jet,

$$L_w = l_w/d_j = f_4(M_j, \gamma_j, p_j/p_d). \tag{22}$$

For a Mach disc, L_w cannot at present be predicted accurately by theoretical methods. Extensive experimental data are available, however, and it is found that L_w increases with p_j/p_d.

In a steady jet flow against a supersonic stream, the jet comes to rest at the free stagnation point. It is assumed here that if there is more than one cell, the jet will continue to develop as the equivalent free jet. In all cases there must be some mechanism by which the jet total pressure is reduced to the free-stream Pitot pressure p_{0f}. If this is accomplished by shock waves, the final shock wave

crossing the axis must be a normal shock. Now it is commonly observed that a stable normal shock does not occur in a region of decelerating flow. A steady terminal shock is therefore restricted to those regions of the equivalent free jet in which the flow is accelerating. In figure 24 + signs are shown on the axis where

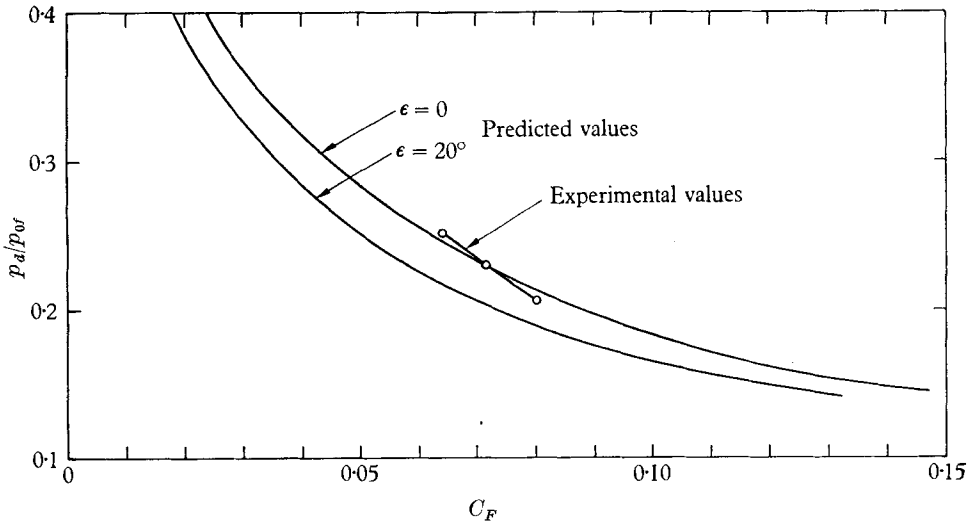

FIGURE 22. Dead-air pressure predicted by the flow model of § 6 compared with experimental values. $M_\infty = 2{\cdot}5$, $M_j = 2{\cdot}6$, $\gamma = 1{\cdot}4$, $\lambda = 1$.

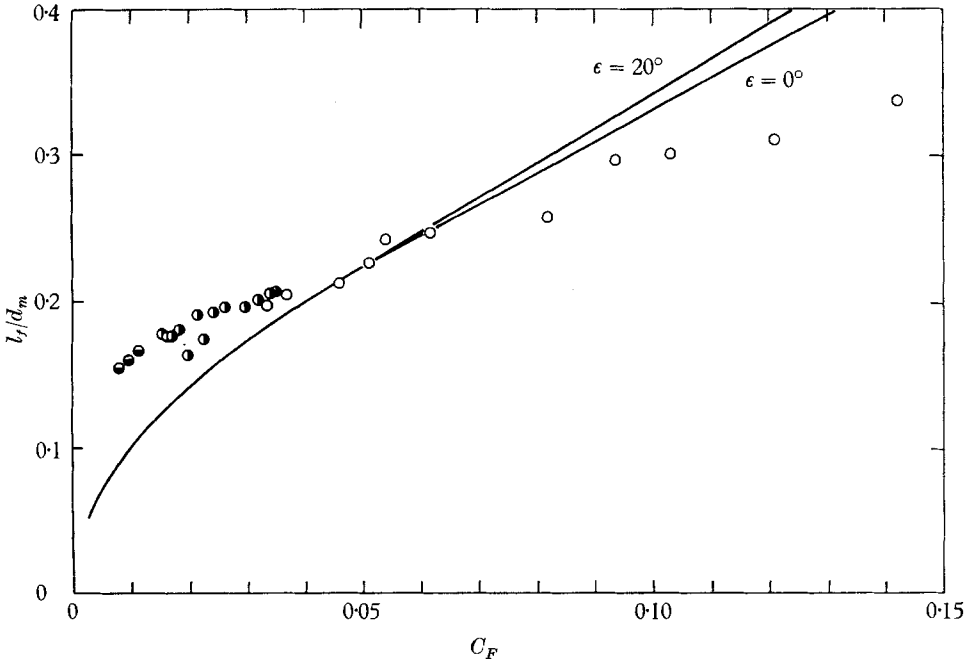

FIGURE 23. Interface position l_f predicted by the flow model compared with experimental values. $M_\infty = 2{\cdot}5$, $M_j = 1$, $\gamma = 1{\cdot}4$, $\lambda = 1$. ——, Predicted values. Experimental values: ○, $D = 7{\cdot}6$; ◑, $D = 16{\cdot}4$; ◒, $D = 33{\cdot}3$.

the flow is accelerating, following the discussion of planar jet structure by Pack (1948). If the terminal shock occurs anywhere downstream of the first jet cell, then the flow entering it depends on p_j/p_d. If it occurs in the first jet cell, the approaching flow is independent of p_j/p_d, also it is the only shock crossing the

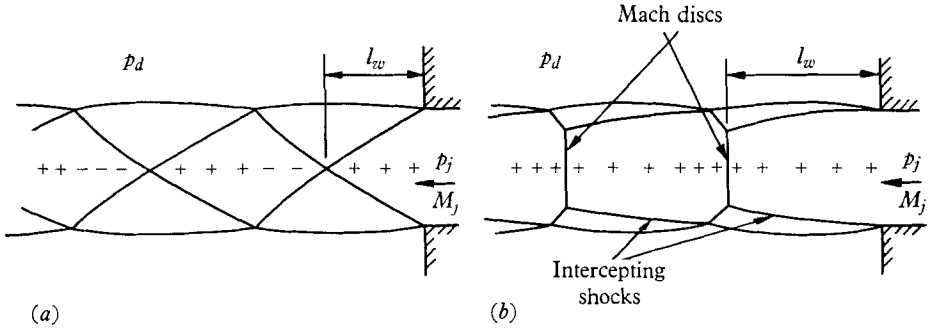

FIGURE 24. Structure of an underexpanded jet.
(*a*) 'Regular' reflexion; (*b*) 'Mach-disc' reflexion.

axis and is responsible for the whole of the required reduction of jet total pressure. This is the case described in § 6.3, with the distance l_s of the shock from the nozzle exit determined by p_{0j}/p_{0f}, M_j and γ_j

$$L_s = l_s/d_j = f_5(P, M_j, \gamma_j). \tag{23}$$

The analysis of § 6 shows that p_d depends on the length of the jet. If the terminal shock occurs in the first cell of the equivalent free jet ($L_s < L_w$) it is unaffected by any change in p_d which may be brought about by a change in the length of the jet. If, however, the terminal shock occurs downstream of the first cell of the equivalent free jet ($L_s > L_w$) a change in p_d will influence the position of the shock, and so the length of the jet, and a closed-loop oscillation mechanism is established. A sufficient condition for steadiness (though not in fact a necessary one, as will be shown later) is that L_w should be greater than L_s. That is

$$L_w(M_j, \gamma_j, p_j/p_d) > L_s(P, M_j, \gamma_j). \tag{24}$$

Now $p_j/p_d = (p_j/p_{0j})\,(p_{0j}/p_{0f})\,(p_{0f}/p_d)$, so that equation (22) may be written

$$L_w = f_6(P, M_j, \gamma_j, p_d/p_{0f}),$$

in which L_w increases as p_d/p_{0f} falls.

An alternative form of (24) is therefore

$$(p_d/p_{0f})_{\max} < \Pi(P, M_j, \gamma_j), \tag{25}$$

where Π is the critical value of p_d/p_{0f} for which the shock position in the jet coincides with the shock position in the equivalent free jet ($L_w = L_s$) or

$$f_6(P, M_j, \gamma_j, \Pi) = f_5(P, M_j, \gamma_j). \tag{26}$$

Figure 25 shows a curve of L_s calculated from Owen & Thornhill's (1952) exact solution for the axial Mach-number distribution of a jet with $M_j = 1{\cdot}0038$ and $\gamma_j = 1{\cdot}4$, exhausting into a vacuum. Experimental results for $M_j = 1$ are also

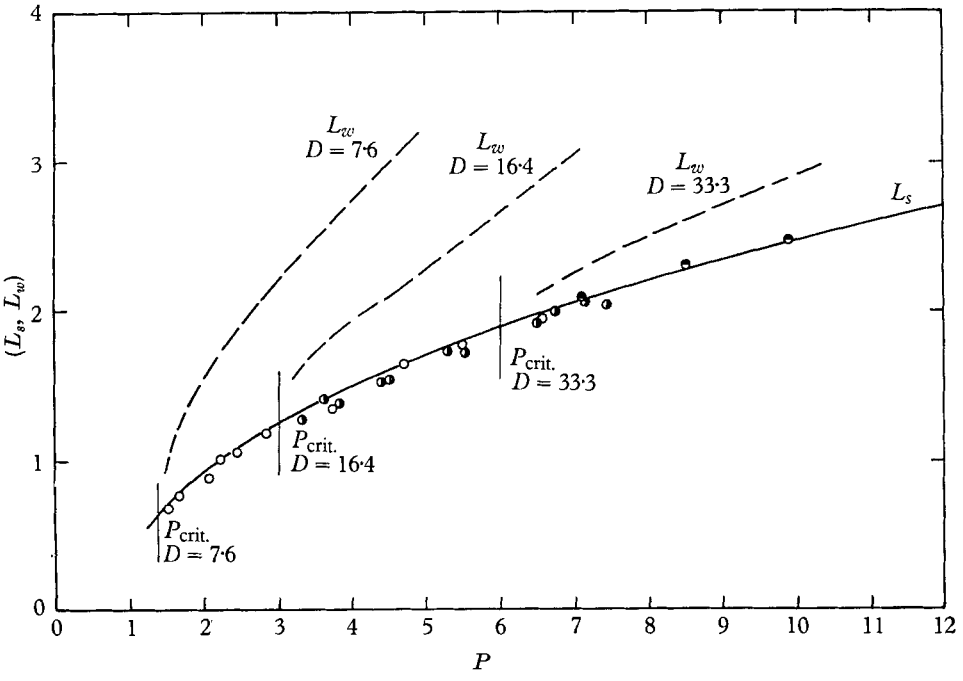

FIGURE 25. Position of jet terminal shock as calculated using Owen & Thornhill's (1952) results, and as measured from photographs. $M_j = 1$, $\gamma = 1{\cdot}4$. ———, Position of the first shock of the equivalent free jet. Experimental values: ○, $D = 7{\cdot}6$; ◑, $D = 16{\cdot}4$; ◓, $D = 33{\cdot}3$.

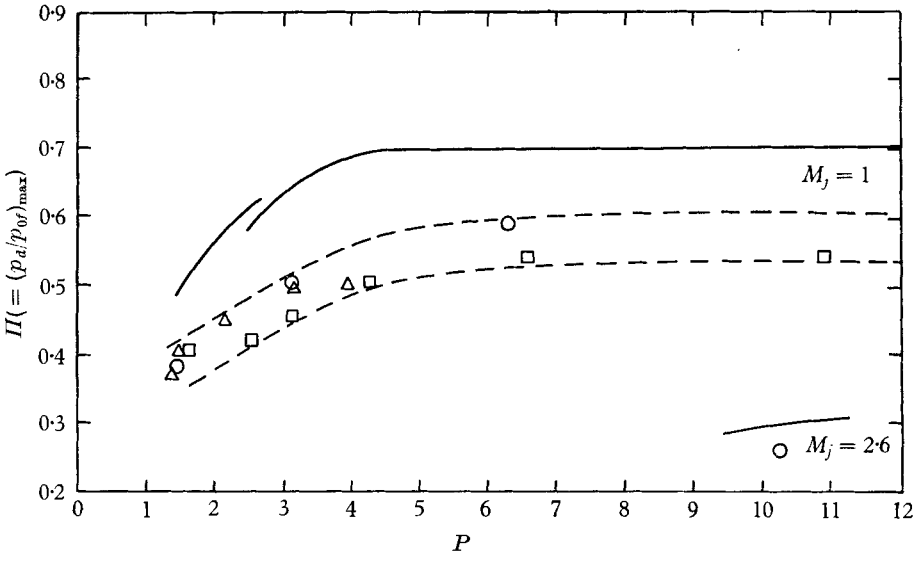

FIGURE 26. Predicted value of the maximum permissible dead-air pressure, and experimental values of the maximum observed mean dead-air pressure. $M_\infty = 2{\cdot}5$, $\gamma = 1{\cdot}4$, $M_j = 1$, 2·6. Predicted values: ——. Experimental values: □, $\lambda = 0$; △, $\lambda = 0{\cdot}5$; ○, $\lambda = 1{\cdot}0$.

shown. They agree very well, with a slight tendency to low values of L_s which may be attributed to the small difference of M_j. Also shown are curves of the variation of L_w with P for each of the large hemispherical models, calculated from the experimental values of p_d/p_{0f} and the experimental data of Love *et al.* (1959) for the shock position in a free jet. It can be seen that L_w approaches L_s as P tends to P_{crit} but does not reach equality.

Figure 26 shows the value of Π calculated from equation (26). (The ambiguity near $P = 2{\cdot}5$ results from slight uncertainty as to when regular reflexion, as in figure 24(*a*), breaks down and is replaced by the Mach reflexion of figure 24(*b*).) Note that Π tends to a nearly constant value at high values of P. The curve for $M_j = 2{\cdot}6$ was obtained using Adamson & Nicholls' (1959) approximate methods. The experimental values of $(p_d/p_{0f})_{\max}$ for regime 3, near P_{crit} are also shown. They lie below Π but form a band of the same general shape, again tending to a constant value at high values of P. The conditions $L_w > L_s$ and $p_d/p_{0f} < \Pi$ are therefore satisfied, but the equalities $L_w = L_s$ and $p_d/p_{0f} = \Pi$ do not predict P_{crit} accurately. The differences are ascribed partly to the fact that p/p_{0f} at the jet boundary is slightly higher than the minimum p/p_{0f} on the model nose which has been arbitrarily identified with p_d/p_{0f} here, but mainly to the presence of small fluctuations in the nominally steady flow. Substantial variations of the dead-air pressure in time are indicated by the considerable range of movement of such flow features as the turning shock (G, figure 3), shown in schlieren photographs such as figures 4(*e*), plate 1, and 9(*b*), plate 2. Thus the experimental values of L_w and $(p_d/p_{0f})_{\max}$ shown in figures 25 and 26 represent time means, and so mark the centre-line of a band. If this band intersects the curves for L_s and Π, the steady flow of regime 3 breaks down.

The levelling-off of Π and the observed $(p_d/p_{0f})_{\max}$ at high P implies a levelling-off in the critical value of C_{FE} also, since p_d/p_{0f} has been shown to depend on C_{FE} only at high P for given M_j and γ_j. It follows that at high values of P

$$P_{\text{crit}} \propto D_E^2. \tag{27}$$

In a range of low values of P, the increase in $(p_d/p_{0f})_{\max}$ with P and the decrease in p_d/p_{0f} with C_{FE} combine to give the observed approximately linear variation of P_{crit} with D or D_E for P less than about 5,

$$P_{\text{crit}} \propto D_E. \tag{28}$$

In figure 27, the observed values of P_{crit} of the present study, taken from figure 12, are plotted against D_E. In calculating D_E from D, the value of α used in equation (20) has been calculated from the experimental value of $(p_d/p_{0f})_{\max}$ as a function of P. Values from previous investigations for which $M_j = 1$ are also shown. In many cases no precise value of P_{crit} can be deduced, and the range within which it lies is then shown by a dotted line. The results plotted cover a range of free-stream Mach numbers M_∞ from 1·5 to 6·0. Body shapes range from $\lambda = 0$ to $\lambda = 6$, and jet gases include helium, nitrogen and carbon dioxide as well as air. The proportional relations of equations (27) and (28) are shown, and agree well with the current data and that of previous workers, if a suitable constant of

proportionality is chosen, agreeing with the present results at $P = 5$. The sufficient condition for steadiness is established and may be stated simply as

$$C_{FE} > C_{FE(\text{crit})} \tag{29}$$

where $C_{FE(\text{crit})}$ is a function of M_j and P, tending to a function of M_j only at high values of P. For $M_j = 1$, the results of the present study suggest that $C_{FE(\text{crit})}$ tends to approximately 0·01.

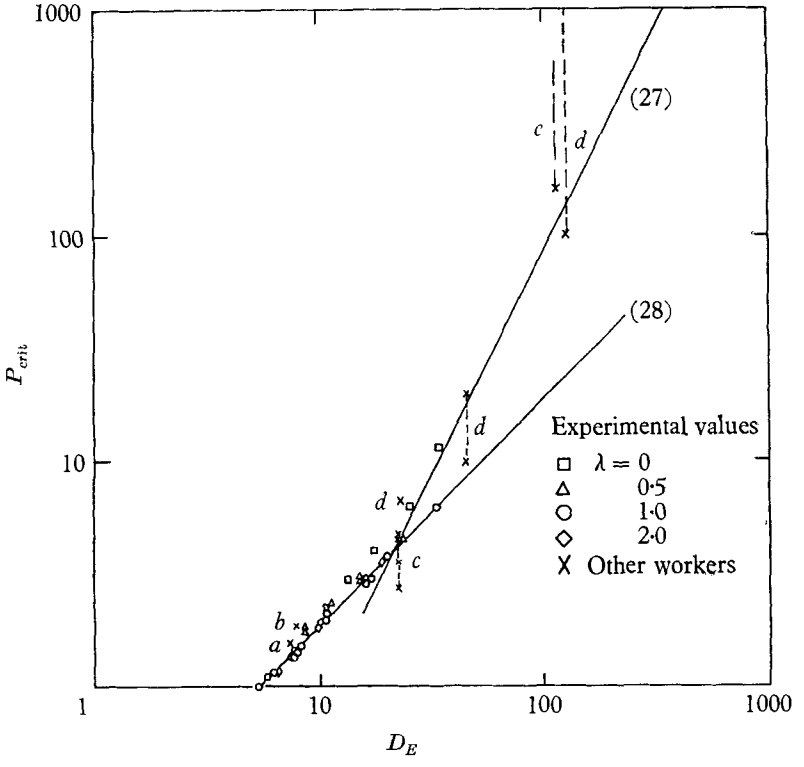

FIGURE 27. Critical total-pressure ratio P_{crit} related to the equivalent body diameter D_E. Experimental values of the present and previous investigations compared to the proportional relations (27) and (28). Experimental values: □, $\lambda = 0$; △, $\lambda = 0{\cdot}5$; ○, $\lambda = 1{\cdot}0$; ◇, $\lambda = 2{\cdot}0$; ×, other workers. *a*, Lopatoff (1951), $M_\infty = 1{\cdot}5$, $M_j = 1$, $\lambda = 6$, air jet; *b*, Love (1952), $M_\infty = 1{\cdot}62$, $M_j = 1, \lambda = 6$, air jet; *c*, MacMahon (1958), $M_\infty = 5{\cdot}8$, $M_j = 1$, $\lambda = 1$, nitrogen and helium jets; *d*, Romeo & Sterret (1963), $M_\infty = 5{\cdot}8$, $M_j = 1$, $\lambda = 1$, air jet; *e*, Charczenko & Hennessy (1961), $M_\infty = 2$, $\lambda = 1$, air jet (calculations based on throat of conical nozzle and $M_j = 1$).

That this sufficient condition is not necessary is shown by the observed existence of the steady flows with multi-celled jets of regime 1. In this case, a closed feedback loop exists, but the feedback is presumably negative. Since no steady multi-celled flow has been observed with a Mach reflexion of the intercepting shocks at the axis, it is suggested that the strong influence of the ambient pressure on the total pressure at the axis in the second and succeeding cells in such cases results in a positive feedback effect. The diagonal shocks of the regular reflexion cause a much smaller drop in total pressure, and correspondingly a small

movement of the shocks will cause little change in the condition of the flow entering a terminal shock in the second or succeeding cells. An alteration of ambient pressure will therefore have a smaller destabilizing effect than for a jet with Mach reflexions, and it is suggested that the steady flow of regime 1 will only exist if a regular reflexion is possible, i.e. if p_j/p_a is less than about 2 for $M_j = 1$. This implies an upper limit for P of about 2, ignoring fluctuations, and a practical limit of about 1·6.

8. Discussion

The experimental results show that the analysis of § 6 describes the steady flows with single-cell jets of regime 3 with fair accuracy. The essential argument is that members of a family of bodies passing through a given jet-orifice position and intersecting a given interface at a specified or negligible angle ϵ are interchangeable, and equivalent to the sphere of that family. The interface and its relation to the orifice are determined by the jet exit Mach number M_j, and a jet flow-force coefficient C_{FE} based on the sphere of the family of bodies. These two quantities include all the principal independent parameters listed at the end of § 2. The other parameters have minor effects which may be predicted as corrections to the correlated experimental data using the analysis of § 6.

It has been shown that the flow can and, in general, will become unsteady if the terminal shock of the jet is influenced by the transport of pressure fluctuations from the dead-air region. This implies that a single-cell jet flow will be steady. Romeo & Sterret (1963) observed the transition from long multi-celled jets in the unsteady-flow regime 2 to the steady single-cell jets of regime 3, and concluded that a single cell was a necessary condition for steadiness. In the long high-Mach-number jets which they studied, the shear layer at the edge of the jet reached the axis in the second cell, and Romeo & Sterret suggested that the unsteadiness of regime 2 was caused by the transport of turbulent fluctuations to the axis. If pursued this argument would lead to the same numerical conclusions as § 7, but would yield a necessary rather than a sufficient condition. That the transport of turbulence is not necessary for unsteadiness can be seen in figure 9(*b*), plate 2, where the unsteady jet is not long enough for the shear layer to have enveloped the axis.

The low pressures in the dead-air region produced by an opposed jet result in a reduction of the forebody drag of a bluff body. The reverse thrust of the jet must be set against this, and it is found that the available net reduction in axial force (ignoring base pressures) depends on the bluntness of the body. Love (1952) and Lopatoff (1951) found that the net reduction of drag for a slender ($\lambda = 6$) body did not exceed 50 % of the reverse thrust applied. If such a body is being propelled by reaction jets, therefore, it remains more economical of thrust to direct the whole available jet thrust to the rear. A simple application of the pressure results of the present study, however, shows that the net reduction of forebody drag for a hemisphere could be of the order of 150 % of the opposed jet thrust when $C_F \simeq 0{\cdot}15$. If such a body were propelled by a rearward-facing jet, aided by a drag-reducing opposed jet, the total thrust requirement could be

about 60 % of that required to propel it by a rearward jet only. If therefore a blunt body, such as, for example, a radome, must be propelled at high Mach numbers, the method appears extremely attractive.

Observations by Ferri & Bloom (1957), Stalder & Inouye (1956), MacMahon (1958), and Warren (1960) have shown that a secondary flow introduced at the nose may reduce appreciably the total heat transfer to a blunt body. Interest in the use of separated jets for this purpose has however declined as a result of Warren's measurement of very high local heating rates in the region of the reattachment zone, which were in some cases even higher than at the stagnation point with no injection. If such a secondary flow is to form a successful 'heat blanket' it must separate the main flow from the body surface to some point rearwards of the stagnation region at reattachment. At the reattachment point the flow will then reach the stagnation temperature of the jet stream, which must have a suitably low value. For this protective approach to be successful the jet layer at reattachment must be thick, so that the shear layer separating the jet from the dead-air region, and that formed on the interface, cannot transport hot fluid from the main stream as far as the dividing stream surface which stagnates at the reattachment point. This implies high values of C_F.

If the integrity of the jet layer is to be preserved, it will also be necessary to ensure that the flow is steady, which again implies high values of C_F. A calculation based on the results of the present study indicated that P_{crit} for the body used by Warren would be about 4·5, and this was only exceeded in one experiment. It seems probable therefore that the high heating rates observed by Warren occurred in unsteady flow with thin jet layers, and that the application of separated jets to heat protection should be re-examined experimentally, using high values of C_F and jets with low total temperatures.

9. Conclusion

The aerodynamic aspects of the flow of a separated jet from a body so as to oppose a supersonic mainstream depend mainly on the Mach number of the jet and a jet flow-force coefficient. A steady flow is obtained when the flow force coefficient exceeds a critical value which depends on the jet Mach number. There is reason to re-examine the practical applications of such flows to drag reduction and heat protection for bluff bodies in continuous high speed flight.

The author performed these investigations while working for the degree of Ph.D. at Cambridge University and wishes to thank his supervisor, Mr E. P. Sutton, for his advice and encouragement throughout. He also wishes to thank the Master and Fellows of Emmanuel College for financial assistance.

REFERENCES

Adamson, T. C. & Nicholls, J. A. 1959 On the structure of jets from highly under expanded nozzles into still air. *J. Aero. Sci.* **26**, 16.

Baron, J. R. & Alzner, E. 1963 An experimental investigation of a two layer inviscid shock cap due to blunt body nose injection. *J. Fluid Mech.* **15**, 442.

Benjamin, T. B. 1962 Theory of the vortex breakdown phenomenon. *J. Fluid Mech.* **14**, 593.

CHAPMAN, D. R., KUEHN, D. M. & LARSON, K. H. 1957 Investigation of separated flows in supersonic and subsonic streams with emphasis on the effect of transition. *NACA Rep.* no. 1356.

CHARCZENKO, N. & HENNESSY, K. W. 1961 Investigation of a retro rocket exhausting from the nose of a blunt body into a supersonic free stream. *NASA TN*, no. D-751.

COOKE, J. C. 1963 Separated supersonic flow. *RAE TN Aero* 2879, *ARC* **24** 935 (unpublished).

FERRI, A. & BLOOM, A. 1957 Cooling by jets directed upstream in hypersonic flow. *WADC TN*, no. 56-382, ASTIA AD 97232.

FINLEY, P. J. 1963 Experiments on jets directed from blunt bodies against a supersonic airstream. Ph.D. Thesis, Cambridge University.

HARTMANN, J. & LAZARUS, F. 1941 The airjet with a velocity exceeding that of sound. *Phil. Mag.* (7), **31**, 35.

LOPATOFF, M. 1951 Wingflow study of pressure drag reduction at transonic speed by projecting a jet of air from the nose of a prolate spheroid of fineness ratio 6. *NACA RM*, no. L 51E09.

LOVE, E. S. 1952 The effects of a small jet of air exhausting from the nose of a body of revolution in supersonic flow. *NACA RM*, no. L 52119a.

LOVE, E. S. 1957 A re-examination of the use of simple concepts for predicting the shape and location of detached shock waves. *NACA TN*, no. 4170.

LOVE, E. S., GRIGSBY, C. E., LEE, L. P. & WOODLING, M. J. 1959 Experimental and theoretical studies of axisymmetric free jets. *NASA TR*, no. R-6.

MACMAHON, H. M. 1958 An experimental study of the effect of mass injection at the stagnation point of a blunt body. *GALCIT Hypersonic Res. Project Memo.* no. 42.

OWEN, P. R. & THORNHILL, C. K. 1952 The flow in an axially symmetric supersonic jet from a nearly sonic orifice into a vacuum. *ARC Rep. & Memo.* no. 2616.

PACK, D. C. 1948 On the formation of shock waves in supersonic gas jets (two dimensional flow). *Quart. J. Mech. Appl. Math.* **1**, 1.

ROMEO, D. J. & STERRET, J. R. 1963 Exploratory investigation of the effect of a forward-facing jet on the bow shock of a blunt body in a Mach number 6 free stream. *NASA TN*, D-1605.

STALDER, J. R. & INOUYE, M. 1956 A method of reducing heat transfer to blunt bodies by air injection. *NACA RM*, no. A56B27a.

SUTTON, E. P. & FINLEY, P. J. 1964 The flow of a jet from the nose of an axisymmetric body in a supersonic airstream. *Archiwum Mechaniki Stosowanej* **3**, 781.

WARREN, C. H. E. 1960 An experimental investigation of the effect of ejecting a coolant gas at the nose of a bluff body. *J. Fluid Mech.* **8**, 400.

WATTS, G. A. 1956 An experimental investigation of a sonic jet directed upstream against a uniform supersonic flow. *UTIA TN*, no. 7.

VAN DYKE, M. & GORDON, H. D. 1959 Supersonic flow past a family of blunt axisymmetric bodies. *NASA TR*, no. R-1.

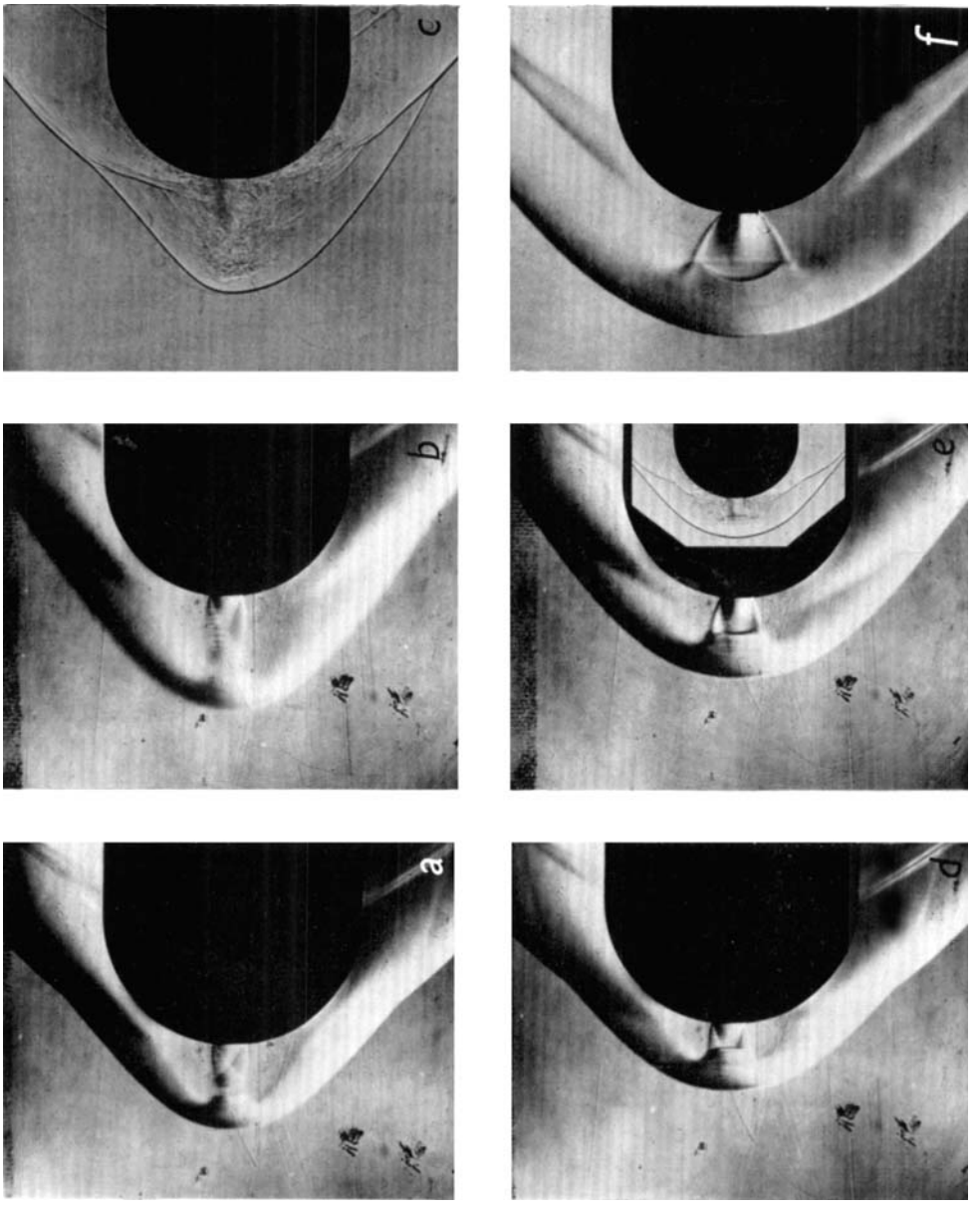

FIGURE 4. Schlieren photographs of the flow about a hemispherical model. $M_\infty = 2{\cdot}5$, $M_j = 1$, $\gamma = 1{\cdot}4$, $D = 7{\cdot}6$.
(*a*) $P = 1{\cdot}08$. (*b*) $P = 1{\cdot}31$. (*c*) $P = 1{\cdot}31$. (*d*) $P = 1{\cdot}68$. (*e*) $P = 2{\cdot}80$. (*f*) $P = 6{\cdot}54$.

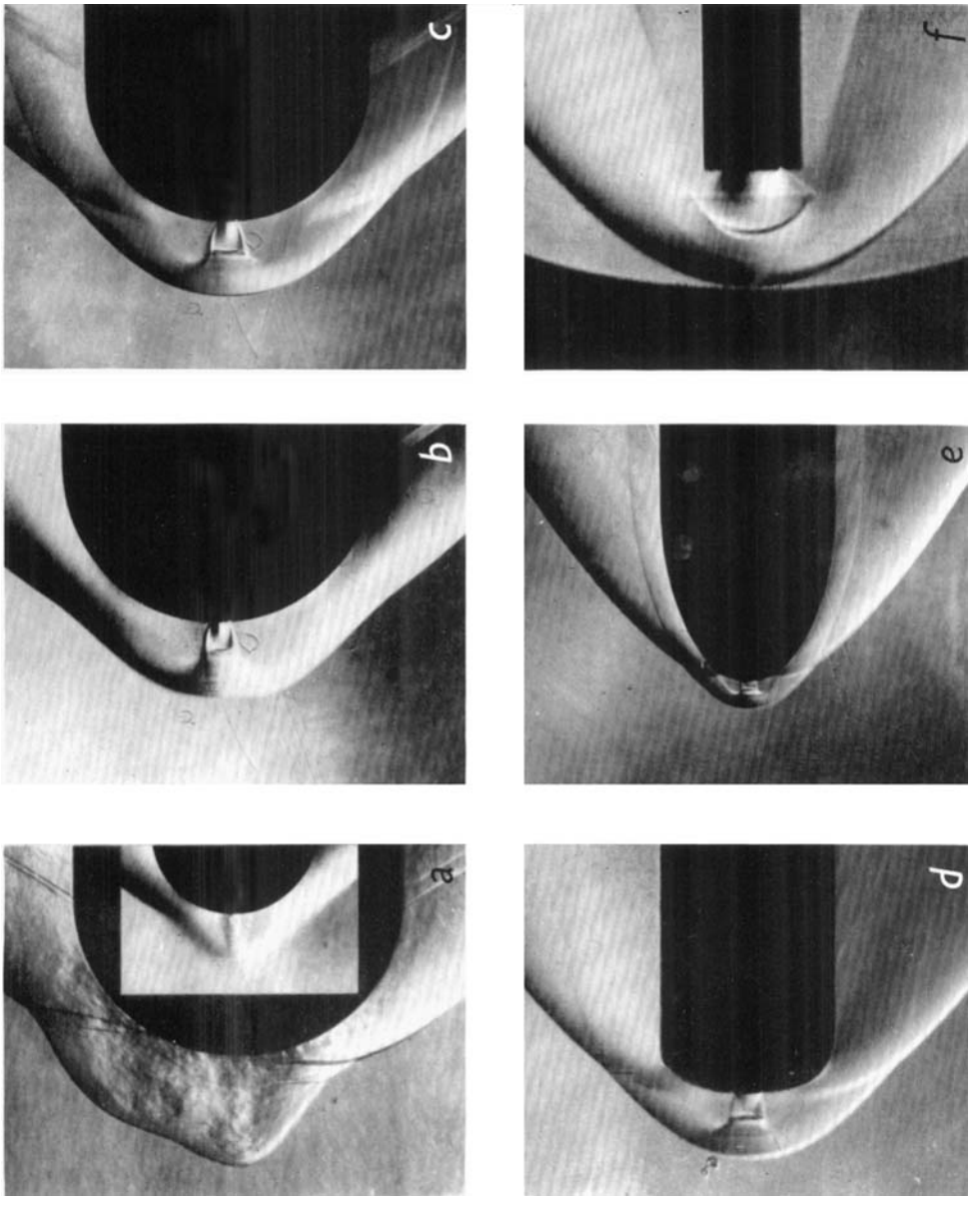

FIGURE 9. Schlieren photographs of the flow about a hemispherical model, $D = 16{\cdot}4$, and various spheroidal models. $M_\infty = 2{\cdot}5$, $M_j = 1$, $\gamma = 1{\cdot}4$. (*a*) $P = 1{\cdot}80$. (*b*) $P = 4{\cdot}50$. (*c*) $P = 6{\cdot}25$. (*d*) $\lambda = 0{\cdot}5$, $D = 6{\cdot}4$, $P = 2{\cdot}25$. (*e*) $\lambda = 2$, $D = 10{\cdot}7$, $P = 2{\cdot}25$. (*f*) $\lambda = 0$, $D = 1{\cdot}67$, $P = 3{\cdot}25$.